IGC Newsletter

Technical Articles
- Studies Towards Raising FBTR Power to 40 MWt
- A Factorial Design Approach for the Synthesis of Phase Pure $AgInO_2$

Young Officer's Forum
- Patch Antenna Design for Wireless Channel Monitors

Young Researcher's Forum
- Nano-spectroscopic and Nanoscopic Imaging of Single GaN Nanowire
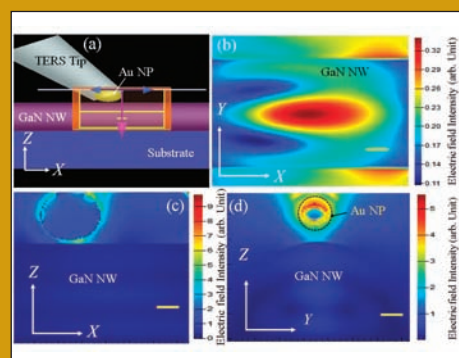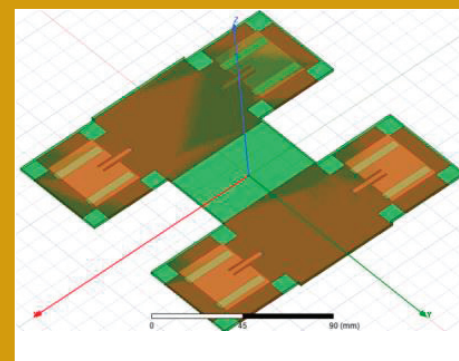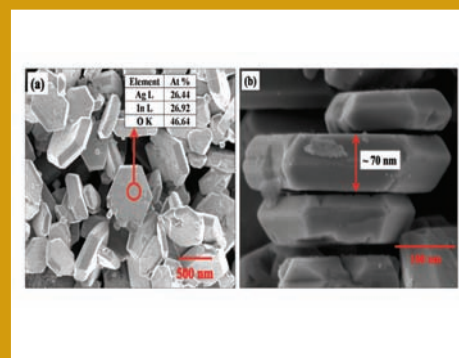
Conference and Meeting Highlights
- ISNT Level II Certification Programme in Visual Testing
- All India Hindi Scientific Seminar (AIHSS-2020)
- Workshop on "Planning, Preparedness and Response to Radiation Emergencies for Medical and Security Officers"
- One Day Workshop on RFID Technology for Libraries
- 4th Discussion Meeting with Collaborative Institutes/Labs on Indian AUSC Projects, Kalpakkam

News and Events
- Swachhta Pakhwada - 2020
- Orientation Program for Engineers and Supervisors involved in Construction

HBNI-IGCAR Corner

Awards & Honours

From the Editorial Committee

Dear Reader

It is our pleasant privilege to forward a copy of the latest issue of IGC Newsletter (Volume 124, April 2020 issue).

In the first technical article, Shri S. Raghupathy and colleagues, Reactor Design & Technology Group have discussed about the "Studies Towards Raising FBTR Power to 40 MWt ".

In the second technical article, Shri A. Sreeramamurthy and colleagues, Materials Chemistry & Metal Fuel Cycle Group have investigated and described about "A Factorial Design Approach for the Synthesis of Phase Pure $AgInO_2$".

Shri Sanam Khan, Electronics and Instrumentation Group has described about the "Patch Antenna Design for Wireless Channel Monitors" in the Young Officer's Forum.

This issue's Young Researcher's Forum features an article by Dr. Santanu Kumar Parida, Materials Science Group, wherein he discusses about the "Nano-spectroscopic and Nanoscopic Imaging of Single GaN Nanowire".

We are happy to share with you the awards, honours and distinctions earned by our colleagues.

We look forward to your comments, continued guidance and support.

With best wishes and personal regards

Editorial Committee, IGC Newsletter

Studies Towards Raising FBTR Power to 40 MWt

FBTR core is originally designed to operate at 40 MWt using mixed oxide (MOX) fuel with 30% PuO_2 and 70% UO_2 (85% enriched U). However, due to the non-availability of enriched uranium, mixed carbide fuel (Mark-I (70%PuC+30%UC)) was chosen for the initial core. After first criticality in 1985, the initial core was operated with a maximum power of 10.6 MWt. Subsequent operations have been carried out by adding many variants of carbide and oxide fuel sub-assemblies (FSAs) and increasing the operating linear heat rating (LHR), based on the encouraging post irradiation examination (PIE) results. The plant was operated at the power level of 32 MWt during its 28th campaign. This core had 58 FSAs; 49 Mark-I, 1 Mark-II (55%PuC+45%UC) and 8 MOX (44%PuO_2+56%UO_2).

The power of FBTR is planned to be raised to its design target power of 40 MWt by using Mark-I subassemblies (SAs). The transition to 40 MWt core is proposed to be taken up during the 30th campaign. The envisaged core will have 70 fuel SAs and the peak LHR will remain restricted at 400 W/cm. In order to ensure a minimum shutdown margin of 4200 pcm as per the technical specification for operation, four poison SAs (with 50% B-10 enrichment) in the 2nd ring are added to the existing 6 control rod SAs (B-10 enrichment of 90 %) provided in the 4th ring. The core design studies have been completed and the proposed core configuration with fuel SAs surrounded by Ni reflector, Thoria blanket and steel shielding SAs is shown in Figure 1.

Neutronics Parameters for Safety Analysis

Perturbation worths and kinetic parameters have been estimated for the proposed core using ABBN-93 cross section library (2D analysis). The fuel slumping worth was estimated using a conservative 1/3rd slumping model and a maximum value of 1.12 $/cm was obtained for the 4th channel. It was found that sodium void reactivity worth was -1035 pcm (-3.82 $). The whole core voiding of steel and fuel reduces reactivity by -7 $ and -219 $ respectively. Doppler constant was found to be -47 pcm. The estimated effective delayed neutron fraction and prompt neutron lifetime are 271 pcm and 0.16 μs respectively. These data form the major inputs for the safety analysis, plant dynamics analysis and severe accident analysis.

Shielding Studies

In the proposed 40 MWt core, the fuel SA boundary would extend up to 24.14 cm in the radial direction with 70 Mark-I sub-assemblies whereas, the core boundary for the existing 32 MWt core is 21.82 cm. The reduction in nickel reflector thickness and the increase in core size have been studied in terms of neutron and gamma flux, dose rates, heating, total dose, radiation damage and helium production.

Calculations have been performed using 2D transport code DORT in RZ geometry using multigroup cross section set IGC-S3. The neutron energy ranges from 10^{-5} eV to 19.6 MeV whereas that of gamma flux is from 1.0 keV to 50 MeV. IGC-S3 is a 217 (175 neutron groups and 42 gamma groups) neutron-gamma coupled cross section set developed in IGCAR from ENDFB-VI in VITAMIN-J structure.

The axi-symmetric (R-Z) model extends up to the biological shielding radially and from grid plate to top shield axially, which is divided into $\sim10^5$ meshes for the calculation. Vacuum boundary condition is used at the bottom, top and right ends, whereas reflective boundary condition is used at the left end. The angular approximation used is S_8 and the order of scattering cross section
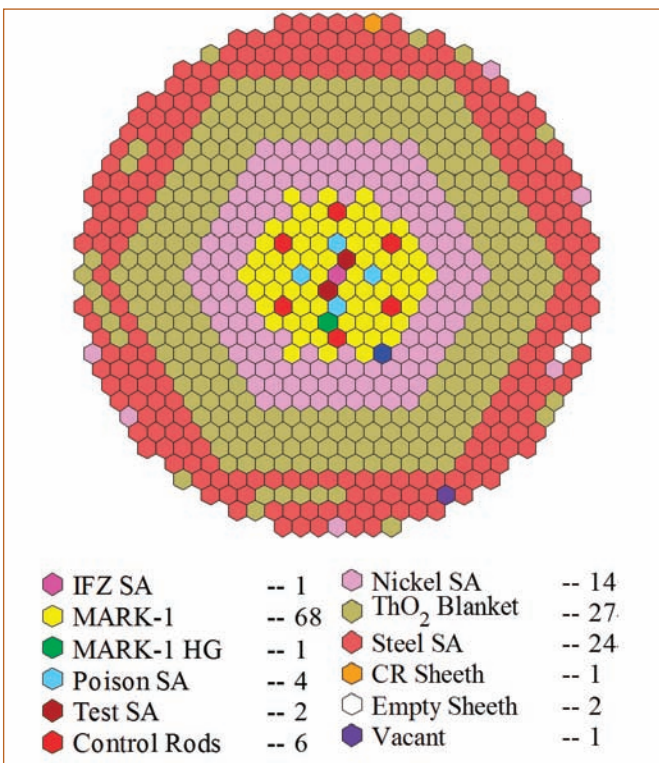

● IFZ SA	-- 1	○ Nickel SA	-- 14	
● MARK-1	-- 68	ThO_2 Blanket	-- 27	
● MARK-1 HG	-- 1	● Steel SA	-- 24	
● Poison SA	-- 4	○ CR Sheath	-- 1	
● Test SA	-- 2	○ Empty Sheath	-- 2	
● Control Rods	-- 6	● Vacant	-- 1	

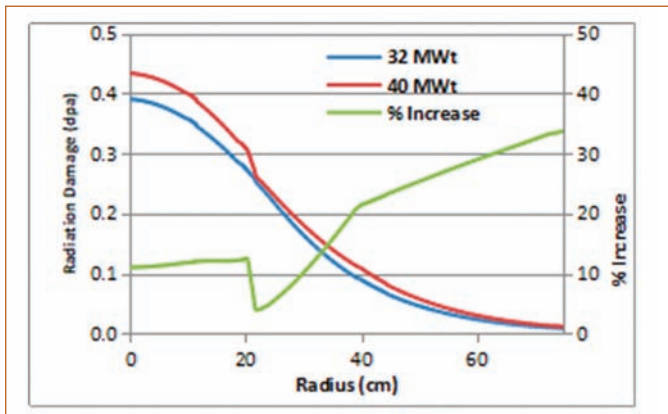Figure 1: Proposed FBTR 40 MWt Core Configuration

Figure 2: Radial Variation of Dose at Grid Plate

anisotropy is P_5. The core centre flux is 3.3×10^{15} n/cm^2/sec which is almost same as that of the present core.

Results show that in general, there was an increase in neutron and gamma fluxes at various locations of the core and shield regions with respect to the 32 MWt core. At the reactor vault exit location, an increase in neutron flux and neutron dose level of 50 % is observed whereas the increase of gamma flux and gamma dose are of the order of 40 %. Similarly, increase in neutron flux and neutron dose level was 20 % whereas that of gamma flux is 30 % at the top shield exit location. During normal operation, increase in cover gas activity was estimated as ~40 %.

The increase in radiation damage rate (in dpa) seen by the grid plate was 11% at the centre of grid plate top region. Based on the limit of 6.3 dpa for the grid plate, the residual life of grid plate reduces from 8.14 full power year (fpy) to 7.25 fpy. The variation of dpa along the grid plate in the radial direction is given in Figure 2.

The increase in helium production is 32 % in the core cover plate. But with 1477 effective full power days of operation so far, core cover plate has already experienced 0.3 appm. With 40 MWt core, the helium production rate will be 0.1 appm per fpy. Neutron flux increase in the detector pit location is 40 %. The increase in detector flux to 1.0×10^{11} n/cm^2/s favours 40 MWt operation of FBTR.

The total heating due to neutrons and gamma at the inner radius of reactor vault concrete increases from 7 W/m^3 to 10 W/m^3. Since the biological shield cooling system is designed for 40 MWt, this increase could be accommodated by the existing cooling system. Since the rotating plug region temperature of FBTR is maintained below 130 °C, Wigner energy release from graphite due to the increase in total neutron flux from 4.82×10^{10} to 6.40×10^{10} n/cm^2/s will not have any significant effect. Since the grid plate dpa is

governing, FBTR is safe to operate for another 7.25 fpy at 40 MWt. **Safety and Severe Accident Studies.**

The kinetic parameters like delayed neutron fractions, decay constants and prompt neutron generation time are estimated for the 40 MWt core. Using the ABBN-93, the isothermal temperature coefficient was estimated as -1.626 pcm/°C and the power coefficient as -5.744 pcm/MWt. However, these coefficients will be measured before power operation.

Hypothetical Core Disruptive Accidents (HCDAs) have been analysed for three accident situations: Unprotected Loss of Flow Accident (ULOFA), Unprotected Transient Over Power Accident (UTOPA) and Unprotected Loss of Coolant Accident (ULOCA). The accident potential of these transients and the associated HCDA energy release have been studied. The accident analyses are carried out through pre-disassembly, disassembly and mechanical energy release phases. The space dependent reactivity feedbacks from the fuel, clad and coolant are taken into account together with radial expansion of core (with due consideration of spacer pad expansion). The Doppler reactivity worth is negligible for the FBTR core. The integral sodium void worth of this core is - 3.82 $.

In the pre-disassembly phase, the course of the accident is evaluated deterministically until the geometry of fuel pin or FSA is intact. The space dependent reactivity feedbacks from the fuel, clad and coolant are taken into account together with core radial expansion feedback.

The initiating event for ULOFA is loss of power supply to the primary pump and the ensuing flow coast down. In the case of ULOFA, the reactor power falls below the decay heat level with due credit to decay heat removal system, the transient does not lead to core disruptive accident.

Under UTOPA, the reactivity addition due to control rod withdrawal rises the reactor power. Variation of reactor power and net reactivity profile for the transient with time is given in Figure 3. Even with negative reactivity feedback, the net reactivity remains positive due to external reactivity addition and power increases. This leads to coolant boiling and fuel melting. The slumping of molten fuel causes a large positive reactivity addition bringing the core close to super prompt critical. The disassembly phase calculations are done assuming a conservative positive reactivity addition to the molten core.

In the case of ULOCA, heat removal from fuel is assumed to be not available and this leads to coolant boiling, fuel slumping and disassembly.
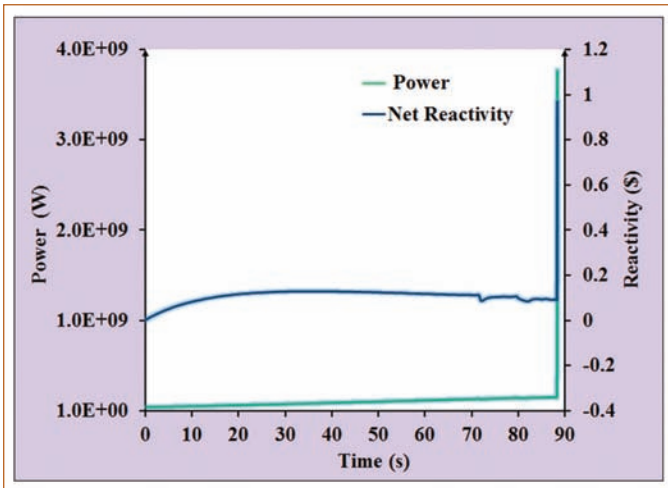
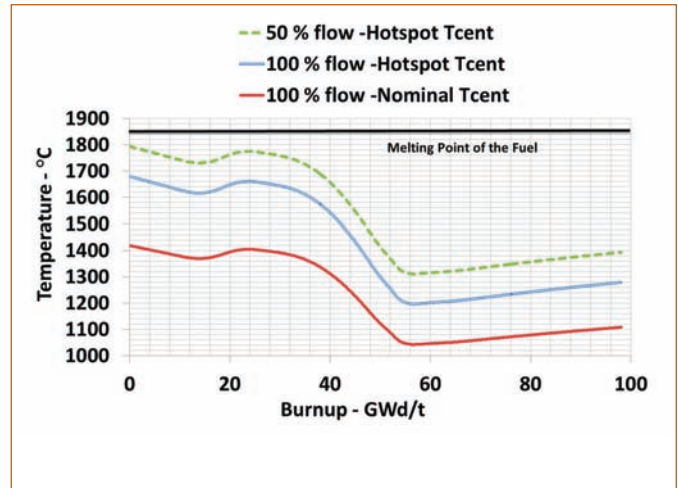Figure 3: Variation of Reactor Power and Reactivity under UTOPA

Figure 4: Fuel Centerline Temperature Variation with Burnup

For conservative reactivity addition rate of 50 $/s input during disassembly phase, the estimated mechanical energy release under UTOPA is 6.9 kJ and under ULOCA, it is 11.94 MJ. Hence, for this core, 12 MJ can be considered as the maximum possible mechanical energy release under HCDA. The reactor vessel can safely withstand up to 9 TNT (39 MJ) of mechanical energy release without failure.

Allowable Flow Reduction in MK-I Fuel Subassemblies Respecting the DSL

The maximum allowable flow reduction in MK-I fuel SAs operating in various rings of FBTR core shall respect the design safety limit (DSL) of fuel and clad. Allowable flow reduction shall be higher than the detectable flow reduction for safe operation of the core.

Clad Temperature: For FBTR core, the third ring fuel SA has the highest LHR which is 374.5 W/cm with a SA power of 625 kW and the corresponding SA flow rate is 3.26 kg/s. The LHR at core top is 238.6 W/cm. For postulated flow reduction, the temperature rise in sodium is found out (including the inter-SA heat transfer) and then the clad mid-wall hotspot temperature is estimated. For the third ring, the clad mid-wall temperature reaches the limit of 800°C when the flow is reduced by 44.5%. For the other rings, allowable flow reduction varies from 44.5% to 53%. Thus, it is concluded that the maximum allowable flow reduction in any ring of fuel SA is 44.5% from clad temperature limit point of view.

Fuel Temperature: The nominal fuel temperature, hotspot fuel temperature with full flow and hotspot fuel temperature with 50 % flow are shown in shown Figure 4 as a function of burnup. The maximum nominal and hotspot centreline temperatures were found to be 1420 ^{o}C and 1680 ^{o}C respectively at core mid-plane at beginning of life (BOL). The hotspot centreline temperature with

50 % flow reduction is 1794 ^{o}C which is well below the melting point of 1850 ^{o}C. Hence, upto a flow reduction of 50 % in the SA, there is no concern over fuel melting. Hence, clad is dictating the flow reduction limit with a maximum allowable flow reduction of 44.5 % in the SA.

Plant Dynamics Analysis

In order to demonstrate the inherent safety characteristics and the capability of plant protection system with respect to various plant transients, analyses of various enveloping design basis events have been carried out using the plant dynamics code DYNAM. It is an in-house developed plant dynamics code validated against commissioning tests carried out in FBTR. The code has models for simulation of neutronic power and thermal hydraulics of primary and secondary sodium circuits. All the enveloping events have been analysed first without crediting of automatic trip triggered by the plant protection system. It was observed that during these events, except 'off-site power failure', 'station black out' and 'one control rod withdrawal', the clad hotspot and fuel hotspot temperatures are limited below the design safety limits even without safety actions demonstrating the inherent safety characteristics of the plant. Moreover, safety of the plant was demonstrated with good margin against the respective design safety limits under off-site power failure, station blackout and one control rod withdrawal events with reactor trip credited based on the second appearing SCRAM parameter. During loss of feed water flow in one loop event, no parameter is available to initiate automatic trip of the reactor. However, there is no concern on core safety during this event even without any safety action. Nevertheless, an additional automatic trip parameter based on high reactor inlet temperature has been proposed to be added to the safety logic.

Another important event towards which safety of the plant is essential to be demonstrated is the single FSA blockage. This analysis is essential for the proposed core configuration due to the introduction of poison SAs which may induce large temperature dilution (due to low heat generation in them) in the measurement of sodium outlet temperature of nearby FSAs. The main objective of the analysis was to estimate the detectable flow reduction in FSAs at various locations in the core. For analysing this event, three dimensional CFD analysis of pool hydraulics in the region above core has been carried out. Typical temperature distribution for the case of a partially blocked SA in the fourth ring is shown in Figure 5. It is seen that the detectable flow reduction in various rings of SAs varies between 9 % and 15 % from center to periphery which are much less than the permissible flow reduction of 44.5 %. Thus, safety of the plant is demonstrated for operation at 40 MWt power.

Poison Subassembly Design

The poison SA consists of a single B_4C rod with plugs welded at both bottom and top. Above and below the rod, hexagonal blocks are kept to increase the weight of the SA to prevent hydraulic lifting. As the poison SA is to be loaded in the fuel region of FBTR core, the foot is designed similar to that of fuel SA. The head of the SA is designed such that its handling is similar to that of a control rod assembly. In order to differentiate poison SA during handling, poison SA length was designed to be 73 mm shorter than the fuel SA. Schematic representation of a poison SA is shown in Figure 6.

Maximum power produced in a poison SA is 35.73 kWt with a peak LHR of 1140 W/cm. The poison SA is designed with a flow rate of 0.409 kg/s. For this flow rate, the maximum clad midwall hotspot temperature and fuel hotspot temperature for nominal power condition are estimated as 538 °C and 2056 °C respectively. The above estimates satisfy the respective design safety limits for nominal and 16% overpower conditions. The sodium temperature rise from inlet to outlet of
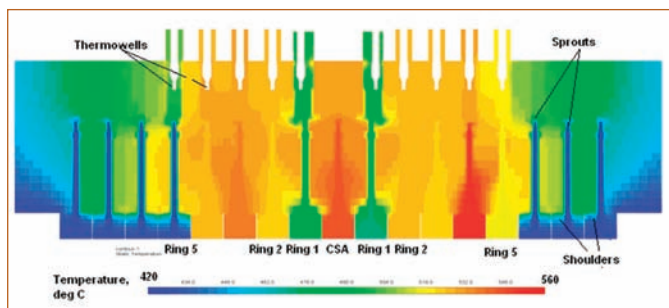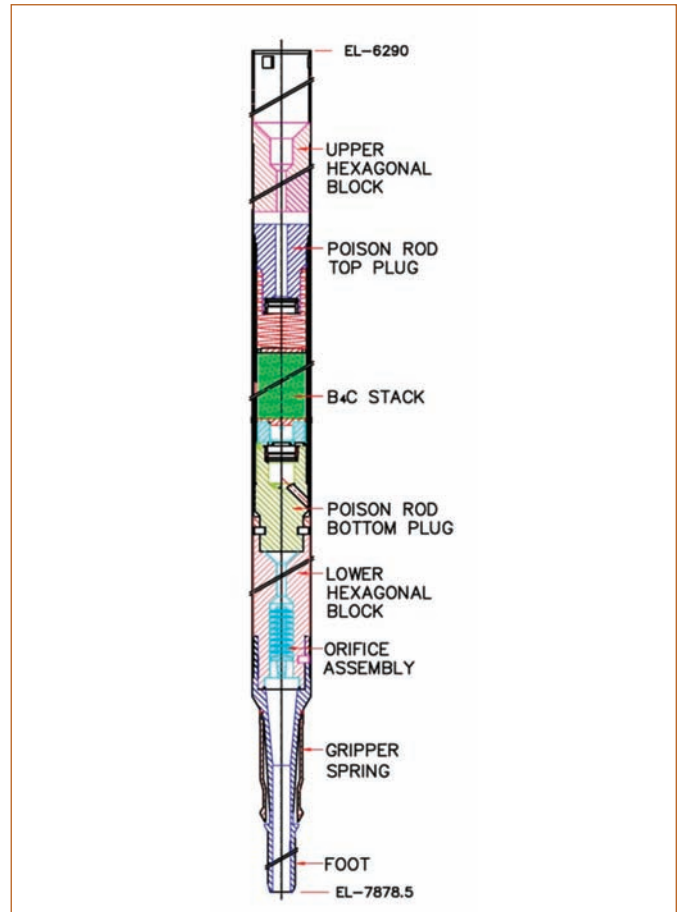
Figure 6: Schematic of FBTR Poison Subassembly

the SA is 97.7 °C which also respects the temperature limits from thermal striping considerations.

The required SA pressure drop of 278 kPa for the designed flow rate is realized by installing comb type labyrinths, orifice structure in the SA foot and also by suitable orificing in upper and lower hexagonal blocks. The above configuration of the flow restricting approach ensures that SA is free from cavitation even at 110% flow condition.

It is planned to raise the power of FBTR to its design target power of 40 MWt with 70 Mark-I subassemblies. Four poison subassemblies are planned to be added in the fourth ring to increase the shutdown margin. Safety studies related to neutronic parameters, protected and un-protected transients have been carried out. Shielding analysis show a slight increase in the dose rates compared to 32 MWt core which is manageable. Based on the various analyses carried out, FBTR is safe to operate for another 7.25 fpy at 40 MWt.

Figure 5: Temperature Distribution in Core Outlet Region under Simulated Blockage of a Fourth Ring SA

Reported by
Shri S. Raghupathy and colleagues, RDTG

A Factorial Design Approach for the Synthesis of Phase Pure AgInO$_2$

AgInO$_2$, a silver delafossite has been reported to form under high temperatures and pressures with residual silver impurity. It is an n-type transparent oxide and has found applications in thermoelectric energy conversion, transparent photo catalysts etc. In this context, we report the formation of phase pure AgInO$_2$ by hydrothermal method using nitrates of silver and indium as starting precursors for the first time by conceiving the factorial design approach to identify the optimum conditions for the synthesis of phase pure product. Three preparative conditions viz., temperature, dwell time (holding time at the reaction temperature) and concentration of KOH with mixed level design were considered for optimization. The coded values for the experimental conditions are shown in Table 1.
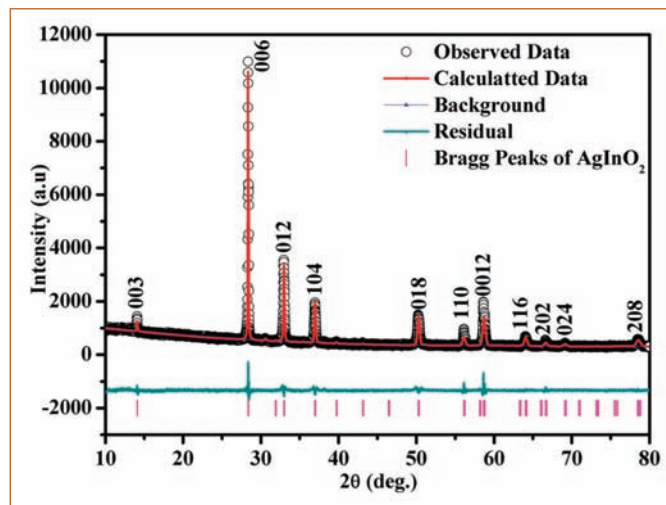

Figure 2: Rietveld refined powder XRD pattern of phase pure AgInO$_2$

Table 1: Coded values of actual experimental conditions considered for the two design matrices				
	Block I		Block II	
Experimental condition/coded value	-1	+1	-1	+1
Temperature ($^\circ$C)	150	180	180	210
Concentration of KOH (M)	4	6	4	6
Dwell time (h)	24	60	24	60

In the current synthesis, stoichiometric amounts of silver and indium in nitric acid media were added to KOH and diluted with water. The mixture was heated to desired temperature under sealed condition for a given time and the product was washed after cooling.

The XRD pattern of the product obtained with hydrothermal conditions of 180 ºC, 4 M KOH and 24 h of dwell time is matching with the rhombohedral R$\overline{3}$m(166) system of AgInO$_2$ (Figure 1) with an increase in relative intensity of (006) to (012) facets (i.e., I(006)/I(012) = 0.40, ICDD # 96-150-9398) to 3.26 indicating texturing. Unit cell parameters, oxygen positional parameter and zero-shift were refined along with background points. Isotropic temperature factors of Ag, In and O were refined in the consecutive refinement cycles. The Rietveld refined X-ray diffraction profile of AgInO$_2$ is shown in Figure 2. The refined unit cell parameters of AgInO$_2$ are found to be a = 3.27668(10) Å and c = 18.8838(7) Å with the unit cell volume of 175.585(14) Å^3. The atomic coordinates of AgInO$_2$ phase are given in Table 2 and the reliability factor of the profile fit as standard Rp, Rwp (Rietveld parameters) values 0.0408 and 0.0570 respectively. The quantitative estimation indicates the presence of no secondary phases.
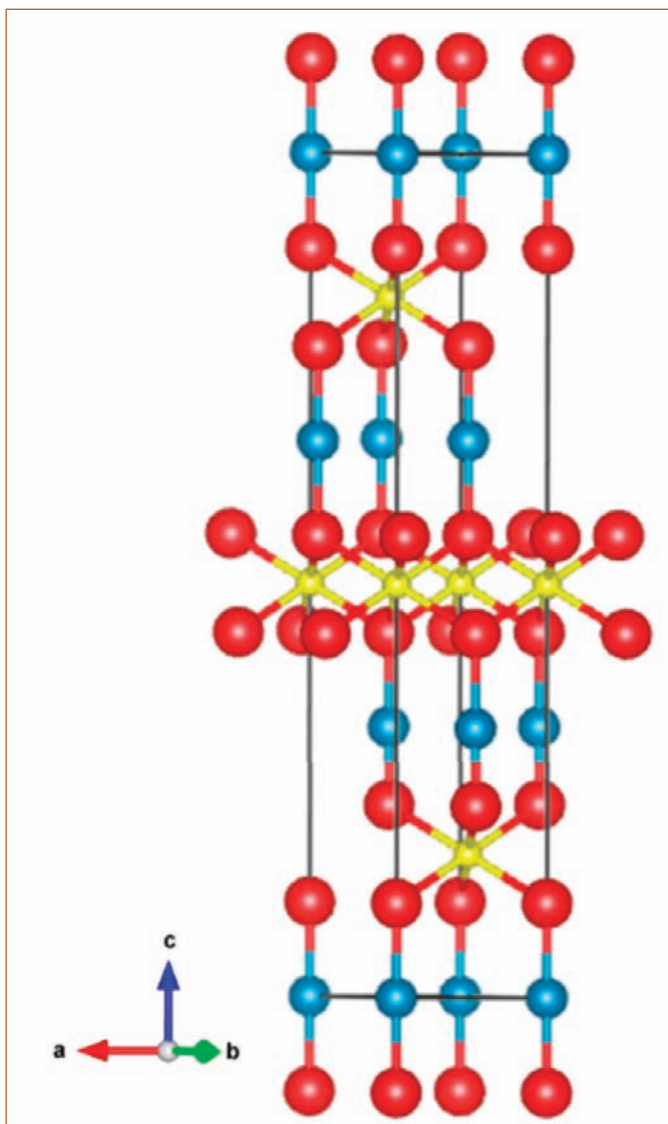

Figure 1: Crystal structure of AgInO$_2$ (blue, yellow & red balls indicate Ag, In & O respectively)

Table 2: Atomic coordinates obtained experimentally from the structural refinement for $AgInO_2$				
Atom	x	y	z	Uiso
Ag	0.0	0.0	0.0	0.0299(28)
In	0.0	0.0	0.5	0.0272(29)
O	0.0	0.0	0.1097(4)	0.025

The sample runs corresponding to 180 °C, 4 M KOH and 24 h or 60 h dwell time yielded phase pure product. The factorial analysis was performed by considering two levels of each factor and splitting the experimental runs into two blocks. Considering response as the fractional intensities of the highly oriented peaks of $AgInO_2$, Ag and In_2O_3 calculated from the X-ray diffraction patterns of the respective samples, two design matrices of two levels each were constructed. A typical design matrix is shown in Table 3. The -1 and +1 are coded values for low and high levels of the different experimental conditions viz., temperature, dwell time and concentration of KOH. The main effects and interactions are calculated and shown in Table 4. In the first block of experiments, the dwell time shows least significance. Even though temperature rise looks like a favorable factor, to the same extent its interaction with the concentration of KOH has opposite effect. Figure 3 represents the combined effect of temperature vs. concentration of KOH, which indicates that 4 M KOH and the temperature of 180 °C are more suitable conditions for the formation of pure $AgInO_2$.

Calculated effects for the second block of experiments indicate that increase in temperature results in the composite mixture instead of pure phase. The high value of temperature effect dominates the positive contribution from interaction terms (AxB and BxC). Overall, the pure phase formation conditions derived from X-ray diffraction intensities suggest 180 °C and 4 M KOH as the best conditions with no dependence on dwell time in the range 24 to 60 h.
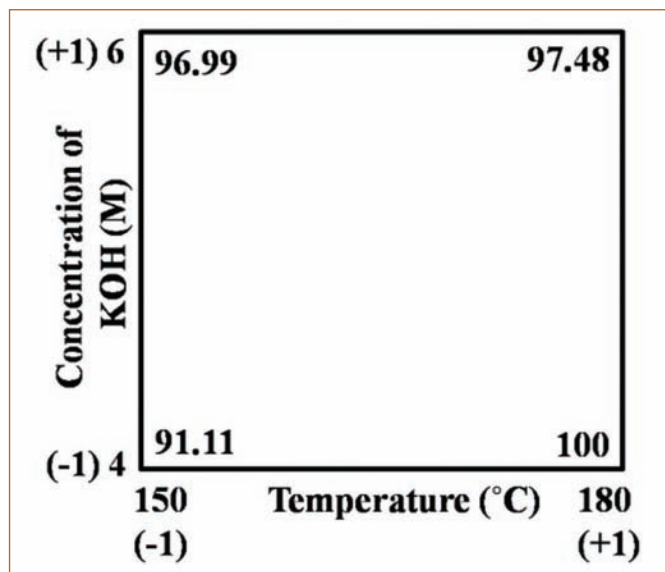

Figure 3: The interaction of temperature and KOH concentration for the first block of experiments. The numbers inside the corners are the average of the responses at respective levels

Table 4: Calculated effects and standard errors for the design matrices. Numbers in bold are of significance for consideration		
	First block of experiments	Second block of experiments
Effect	Estimate ± standard error	Estimate ± standard error
Average	97.31 ± 2.77	90.31 ± 9.19
Main effects Temperature (A)	**3.03 ± 1.88**	**-17.04 ± 1.09**
Concentration of KOH (B)	0.53 ± 1.88	-0.63 ± 1.09
Dwell time (C)	1.83 ± 1.88	-0.27 ± 1.09
Two-factor interactions		
A x B	**-2.88 ± 1.32**	**1.73 ± 0.78**
B x C	-1.15 ±1.32	**0.97 ± 0.78**
C x A	-1.66 ±1.32	-0.44 ± 0.78
Three-factor interactions		
A x B x C	1.32	0.80

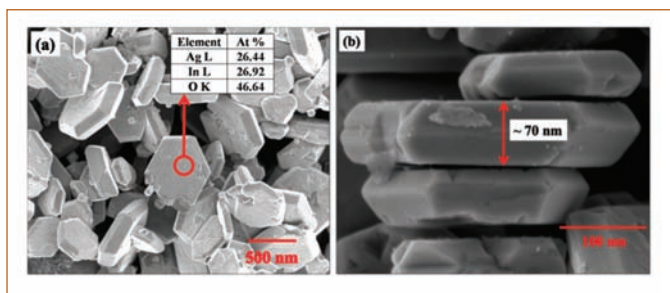| Table 3: Design matrix for the first block of experiments									
Run No.	Intercept	Temperature (A)	Concentration of KOH (B)	Dwell time (C)	A x B	B x C	C x A	A x B x C	Response
1	1	-1	-1	-1	1	1	1	-1	91.11
2	1	-1	-1	1	1	-1	-1	1	97.07
3	1	-1	1	-1	-1	-1	1	1	96.99
4	1	-1	1	1	-1	1	-1	-1	98.01
5	1	1	-1	-1	-1	1	-1	1	100.00
6	1	1	-1	1	-1	-1	1	-1	100.00
7	1	1	1	-1	1	-1	-1	-1	97.48
8	1	1	1	1	1	1	1	1	97.82

Figure 4: FE-SEM images of as-prepared phase pure AgInO$_2$ (run 5) (a) a panorama and (b) side view; Inset corresponding EDX values
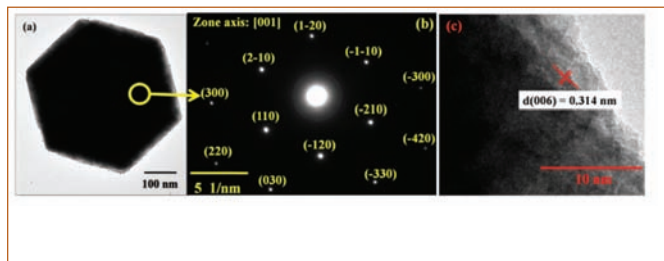

Figure 5: (a) High magnification TEM image of phase pure AgInO$_2$; (b) SAED pattern along the [001] zone axis and (c) high-resolution TEM recorded on the surface of the hexagon

Figure 4(a) and 4(b) shows the FE-SEM images of AgInO$_2$ in panoramic and side views, disclosing the hexagonal-shaped plate like morphology with an average width of $\sim$ 300 nm and thickness of $\sim$ 70 nm. EDX analysis confirmed the atomic ratio of Ag to In as 0.98 (close to stoichiometry), with no evidence of potassium signatures.

The TEM of AgInO$_2$ grain resulted in well-defined facets with a hexagonal plate-like shape (Figure 5(a)). The SAED pattern (Figure 5(b)) on the surface of the hexagon shows diffraction spots along the [001] zone axis, indicating the single crystalline feature of AgInO$_2$ crystals with (1-20), (2-10), (110), and (300) atomic planes that confirms AgInO$_2$ single crystal has exposed planes of (001) in dominance and the results are in concurrence with that of XRD. Figure 5(c) shows a lattice resolved HRTEM image of(006) crystal plane of AgInO$_2$ with a d spacing of 0.314 nm. The percentage fraction of the surface area of the dominantly exposed (001) facets to the total is unusually higher (52 %) than the theoretical estimate of 2 % for isotropic specimen.

XPS survey spectrum of AgInO$_2$ nanoplates indicated the presence of only Ag, In, C and O. The Ag 3d components viz. 3d$_{5/2}$ and 3d$_{3/2}$ at 367.8 and 373.8 eV with a spin orbit coupling parameter

(SOCP) of 6.0 eV attributed to Ag$^+$ state (Figure 6(a)). Similarly, 3d$_{5/2}$ and 3d$_{3/2}$ of Indium with an SOCP of 7.6 eV resulted in peak positions at 444.4 and 452.0 eV respectively (Figure 6(b)) that corresponds to In^{3+}. The O 1s pattern shows three peaks viz., at 529.7, 531.5 and 533.5 eV respectively due to the lattice oxygen, absorbed O^{x-} species and adsorbed moisture or hydroxyl groups(Figure 6(c)).

The specific surface area (S$_{BET}$) of the samples deduced from the N$_2$ adsorption isotherm was about 48.5 m^2 g^{-1}. The optical band gap is estimated to be 2.20 eV from the Tauc plot of absorption spectra (Figure 7). The TG-DTA resulted in a marginal decrease in weight of 0.3 %, possibly due to moisture escape and the compound is found stable up to the temperature of 595 °C. A noticeable weight loss (about $\sim$ 3 %) accompanied by an endothermic peak in the temperature range of 595 – 680 °C indicates the decomposition of AgInO$_2$ into Ag and In$_2$O$_3$.

Figure 8(a) shows the typical Nyquist plots with equivalent circuit in the inset of AgInO$_2$ in air ambient in the temperature range from 160 to 400 °C. The log (σT) vs. (1000/T) profile (Figure8(b)) exhibited Arrhenius behaviour with an activation energy of 0.24 eV/f.u.
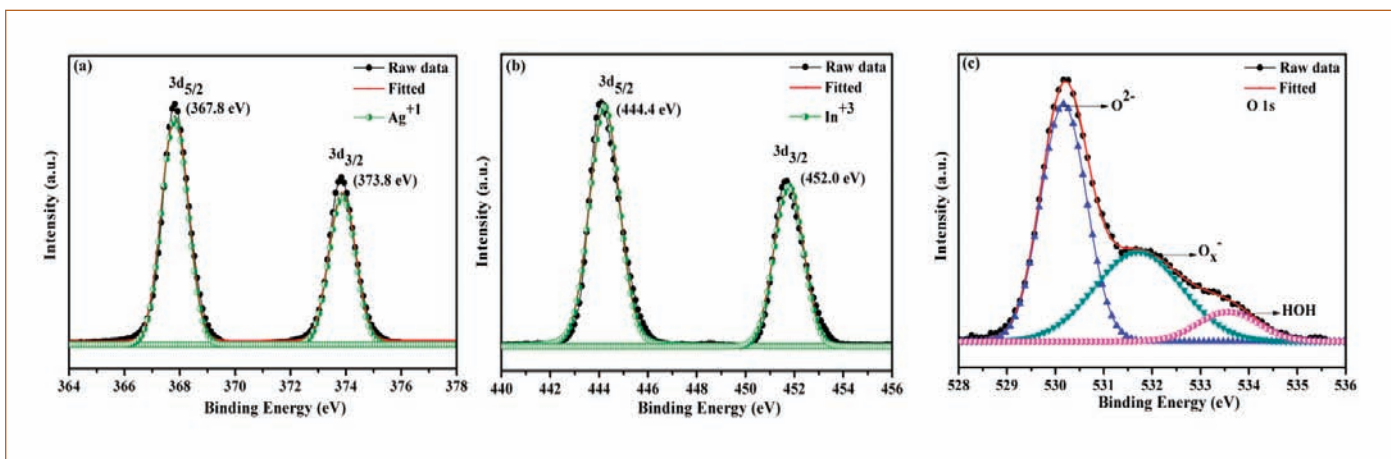

Figure 6: XPS spectra of AgInO$_2$ nanoplates a) Ag 3d, b) In 3d and c) O 1s
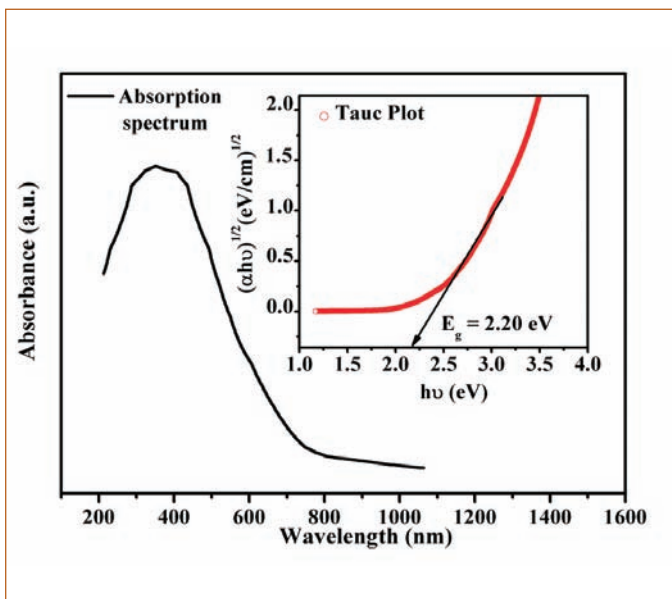
Figure 7: UV - Visible absorption spectrum with tauc plot (inset) of $AgInO_2$

The preliminary step in visualizing the growth of $AgInO_2$ is to suppress the precipitation of metallic silver. This is anticipated by stabilizing the as-precipitated $Ag(OH)_2^-$ by the presence of a large amount of hydroxyl ions in water which necessitates the addition of a strong base. The low probability of K^+ ion into the $AgInO_2$ structure prefers KOH over LiOH/NaOH. Secondly, the solubility of both $Ag(OH)_2^-$ and $In(OH)_3$ in aqueous solution are necessary. The Pourbaix diagrams for $Ag-H_2O$ system over a wide range of temperature ($25 - 300\,°C$) have shown the formation of the aqueous soluble $Ag(OH)_2^-$ species in alkaline medium with Ag^+

solubility notably high ($10^{-2.5}$ mol/L). Similarly, $In(OH)_3$ has the maximum alkaline solubility of 6×10^{-2} mol/L. Moreover, it has been reported that the formation of Ag metal can be suppressed by the presence of KNO_3 in the solution. Thirdly, both $Ag(OH)_2^-$ and $In(OH)_3$ have to be stabilized at processing temperatures of about $150 - 200\,°C$ under hydrothermal conditions. Bomb calorimetric measurements showed the pressures inside the bomb were 4.8, 9.2 and 18 atm at 150, 180 and 210 °C respectively. By optimizing the temperature and pH, the reaction proceeds until all the starting materials are progressively dissolved and leads to the formation of pure $AgInO_2$. Although all the hydrothermal temperatures under study yielded $AgInO_2$, only the sample processed at 180°C and 4 M KOH yielded the phase pure $AgInO_2$.

In conclusion, hexagonal nanoplates of phase pure $AgInO_2$ was successfully prepared via hydrothermal route for the first time by considering a factorial design approach. In this synthesis, the combined effect of 180 ºC and 4 M KOH with no dwell time dependency between 24 h and 60 h are found favorable for phase purity. $AgInO_2$ crystallized in rhombohedral structure with dominantly exposed (00l) facets with Ag, In and oxygen to be +1, +3 and -2 valences respectively. The compound exhibited an activation energy of 0.24 eV/f.u. for electrical conduction and an optical band gap of 2.20 eV with a thermal stability up to 595 ºC in air. It is believed that these experimental investigations will stimulate the synthesis of various delafossite compounds for different applications by factorial design approach.

Reported by
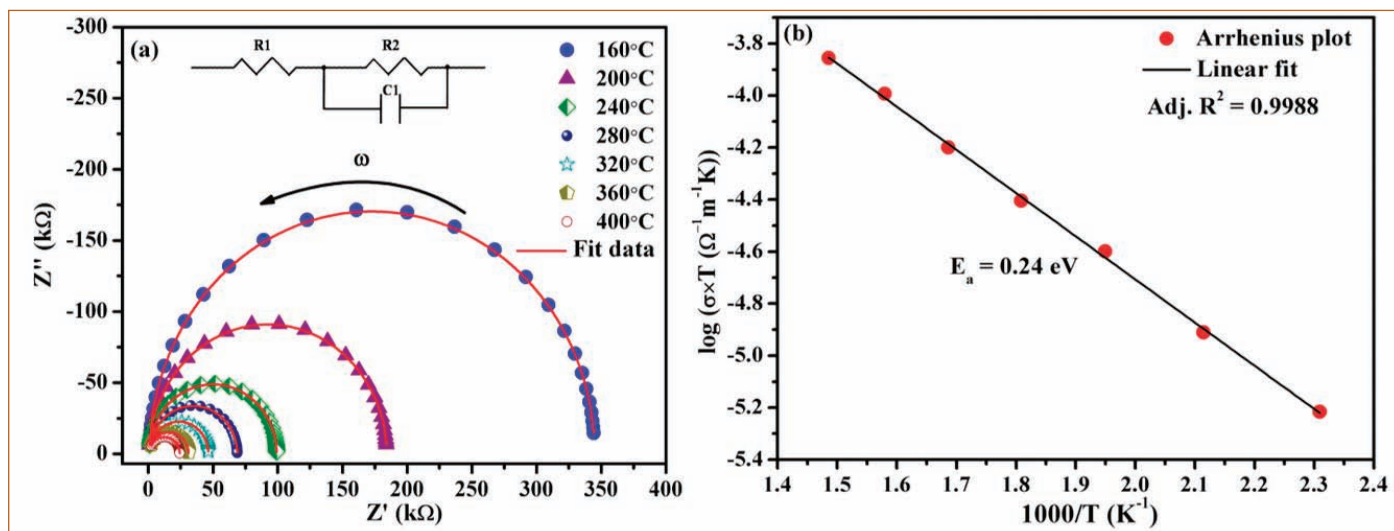*Dr. A. Sree Rama Murthy and colleagues, MC & MFCG*

Figure 8: (a) Nyquist plot of $AgInO_2$ at different temperatures in air; Inset shows the equivalent circuit for fitting the impedance data and (b) log ($\sigma\times$T) vs 1000/T of $AgInO_2$

Young Officer's FORUM

Shri Sanam Khan is working as a Scientific Officer in the Wireless Network Section (WNS) of Computer Division under Electronics and Instrumentation Group (EIG). He is from the 9th batch of BARC Training School at IGCAR campus and is a recipient of the Homi Bhabha award winner in the Electronics & Instrumentation discipline. He obtained his M.Tech in Electronics and Instrumentation from Homi Bhabha National Institute. His current areas of interest comprises acoustic signal processing, vibration monitoring and RF component design for wireless sensor networking applications.

Patch Antenna Design for Wireless Channel Monitors

In the recent times, Wireless Sensor Network (WSN) has become increasingly popular in industries for process parameter monitoring. The WSN can cover hundreds of meters even with the absence of line-of-sight. In nuclear environment, there will be multiple WSN nodes within a confined area, which raise the complexity of handling the wireless traffic without data loss. In such situation, it is mandatory to have an exclusive wireless monitoring and managing system. Managing a network includes monitoring of packet routing, load distribution for individual routers, verifying link quality etc. To assess the above mentioned network attributes, the devices called Wireless Channel Monitors (WCM) are designed and developed.

Commercially available WCMs scan multiple channels by sweeping across various channels of IEEE 802.15.4 spectrum. The main drawback of such channel monitors are high probability of missing network packets. Also, sweeping across all channels sequentially using a single antenna involves time delay and this will certainly lead to packet losses which in turn results in high packet drop ratio. To improve the packet reception probability from the network, one possible solution is to install multiple sniffer modules operating simultaneously. However, hardware complexity will scale up with the monitoring of more number of channels. To overcome all these obstacles and yet combine the advantages of both type of channel monitoring solutions, it has been proposed to design a quad transceiver channel monitor. The special attribute of developed WCM is governed by its ability to monitor simultaneously four different channels or to sweep channels in four defined sub bands of WSN networks. The physical layer of IEEE 802.15.4 based WSN at 2.4GHz band

consist of 16 channels and its entire band can be divided into sub-bands of 4 channels; thus, each transceiver of quad WCM needs to sweep only 4 channels. To reduce the form factor of the quad WCM, microstrip techniques have been incorporated into the design the quad antenna.

The work involved design and development of different types of microstrip antennas, their simulation and practical results. Also, using multiple patch elements, a quad patch antenna was designed, developed and tested for WCM applications. Parameter such as coupling co-efficient has been minimized with suitable design and placement of the patch elements.

1. Antenna Modeling & Simulation

The antenna designs which have been modelled and simulated are – rectangular patch, meander and dipole. These patch structures are standard patch designs because of their simplicity and good antenna attributes. Rectangular patch provides high gain (~5-6 dBi) with directional pattern. Meander structure reduces antenna form factor and at the same time provides omni-directional pattern with reasonable gain. Dipole patch compromises on size but provides with very good gain with omni-directional pattern.

Design of quad antenna for quad WCM involves the following key contributions:

• Initially, individual patch elements were modelled and optimized

• Using the patch elements, the mutual coupling effect of multiple antennas on single substrate has been studied

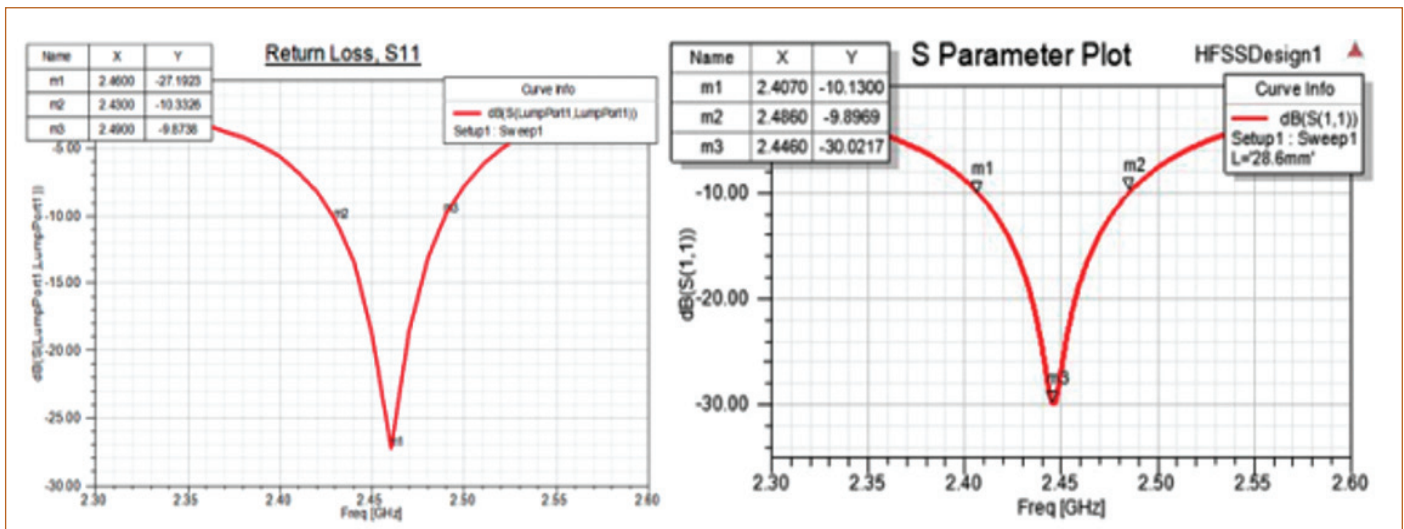• Design of quad antenna was optimised, developed and tested.

Figure 1: Reflection coefficient of Rectangular Patch Antenna without & with DGS

1.1 Rectangular Patch Antenna

Rectangular Patch Antenna is the basic design of microstrip antenna. Dimensional calculations were done for the basic design antenna and its bandwidth is found to be 60 MHz which is much lower than the desired bandwidth as specified by the physical layer of IEEE 802.15.4.

To achieve the desired bandwidth with improved gain, modifications need to be done in the basic antenna design. By theoretical studies, it is proved that, the change in the ground (GND) plane pattern of the microstrip patch antenna will result in change in bandwidth and gain. Hence various modifications in GND plane have been tried. This method to improve antenna parameters is referred to as Defective Ground Structure (DGS) implementation. Each DGS shape has its own characteristics and

creates effect on the performance of the device according to its geometry and size.

In the basic design antenna, at the four corners of GND plane, patches of size 9.6 x 9.6 mm^2 were stripped off based on optimetrics analysis. Beneath the radiating patch element, two rectangular patches were also removed from GND plane. The effect of the modifications were tested and found that the bandwidth is 86 MHz, which is a substantial improvement over the previous design. Centre frequency is observed to be 2.446 GHz while maximum gain is found to be 3.95 dB. Hence it can be considered for constructing the quad antenna. Figure 1 shows the reflection co-efficient of Rectangular Patch Antenna without & with DGS.
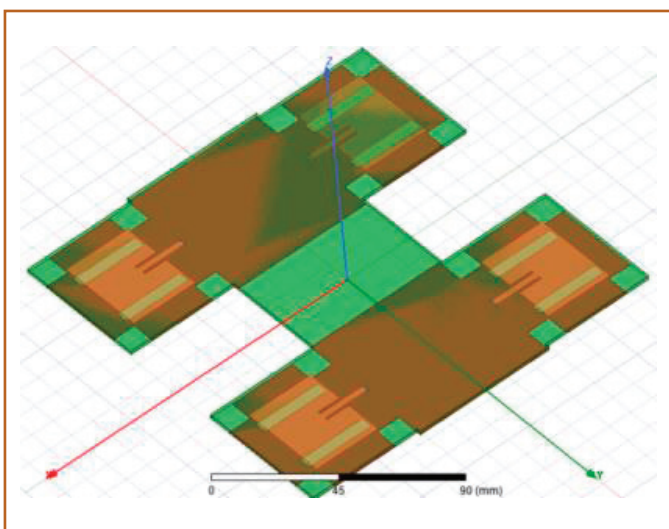
1.1.1 Rectangular Patch Based Quad Antenna

Using the rectangular patch element, quad antenna has been designed by placing 4 rectangular patch antennas with DGS on a single substrate. Simulation has been carried out to identify maximum cross-coupling possible in this design. Figure 2 shows the Quad antenna using Rectangular Patch Antenna with DGS.

From the S parameter plot, maximum cross- coupling was found to be -17. 63 dB.

In quad antenna design, all the constituent patch elements are of directional type. To explore omni-directional type patch based quad patch antenna, at first different types of patch elements were designed to find the best suited candidate.

1.2 Meander Patch Antenna

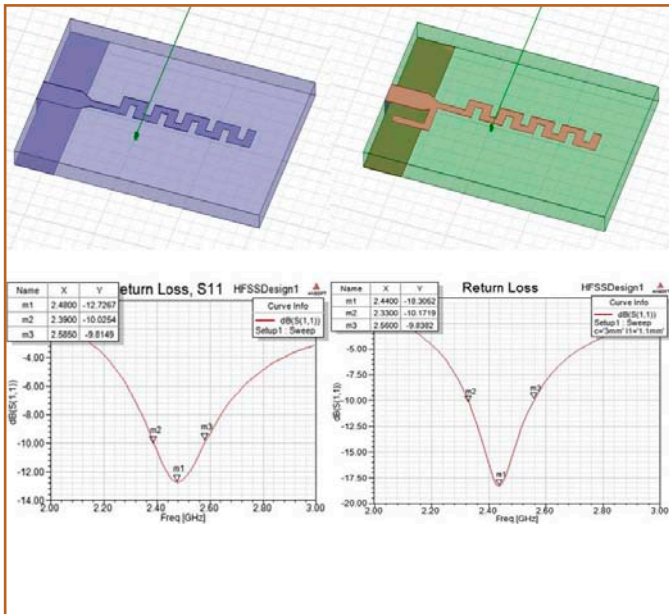Meander pattern is used to design compact patch antenna with

Figure 2: Quad antenna using Rectangular Patch Antenna with DGS

Figure 3: Meander patch antenna with and without stub (top) and their reflection coefficient (bottom) respectively

Figure 4: PCB dipole antenna with reflection coefficient plot

omni-directional radiation characteristics. Folding a simple monopole antenna back and forth increases the compactness of the antenna without compromising on resonance frequency. Here, the designed meander antenna is of type monopole. In this design, tapered feed has been used to improve discontinuity in the structure. From Figure 3, antenna operating center frequency is observed to be 2.48 GHz with a bandwidth of 195 MHz. Antenna gain for this meander antenna is found to be 2.09 dB with a maximum return loss of -12.7 dB, which implies poor matching between the feed and the radiating elements.

To improve upon impedance matching, open ended stub has been incorporated. Stub matches are widely used to match any complex load to a transmission line. They consist of shorted or opened segments of the line, connected in parallel or in series with the line at an appropriate distance from the load. At first, optimetrics study was performed to figure out exact length of the stub and distance from the load at which it is to be connected. Design and the results observed after design optimization are shown in Figure 3. From the figure, it can be observed that the return loss has increased substantially (-18.3 dB). For this design, the achievable bandwidth is 230 MHz.

Parameters of practical monopole antenna suffer from the effect of finite size ground plane. This effect was observed while performing practical testing of antennas using vector network analyser. Besides, the realized gain was also found to be 1.99 dB.
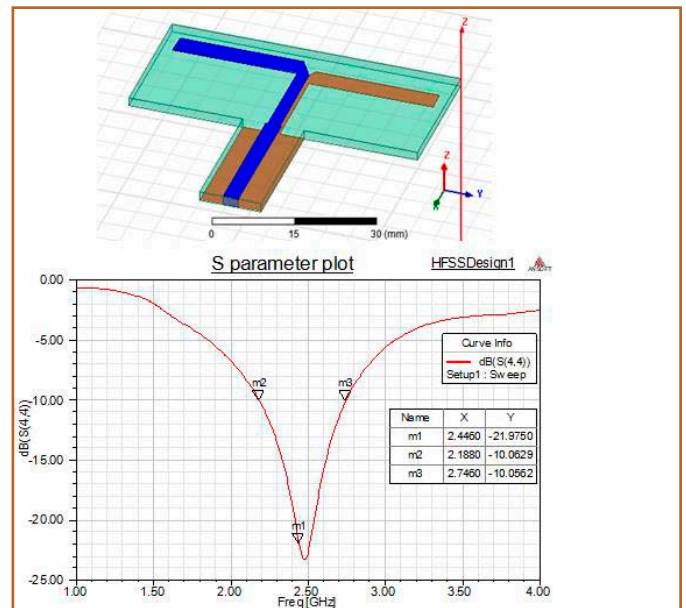
1.3 Dipole Patch Antenna

To improve the gain bandwidth product and reduce the effect of finite ground plane, PCB dipole antenna has been designed. This section focuses on the analysis, design, and fabrication of 2.4 GHz dipole antenna on PCB substrate. The antenna is fabricated on two sides of the FR4 substrate (with dielectric constant 4.4) and connected to a "balanced-to-unbalanced" line (BALUN). The microstrip BALUN compels the flow of current to get equally distributed in both arms of the dipole, thus increasing the radiation efficiency. Design and the results observed are shown in Figure 4.

As can be observed from Figure 4, a substantial improvement in bandwidth (300 MHz) and gain (2.7 dB) makes this antenna a suitable candidate to be used for designing quad antenna for WCM.

1.4 PCB Dipole Based Quad Antenna

As discussed earlier, quad antennas are four patch antenna elements, printed in a single substrate, with each one of those would be operating in different channels of IEEE 802.15.4 for simultaneous sniffing of multiple RF packets.

To minimize the cross coupling among patch elements, two types of placements have been explored, termed as parallel and plus. Figure 5 (top left & top right) demonstrates the parallel and plus design respectively.

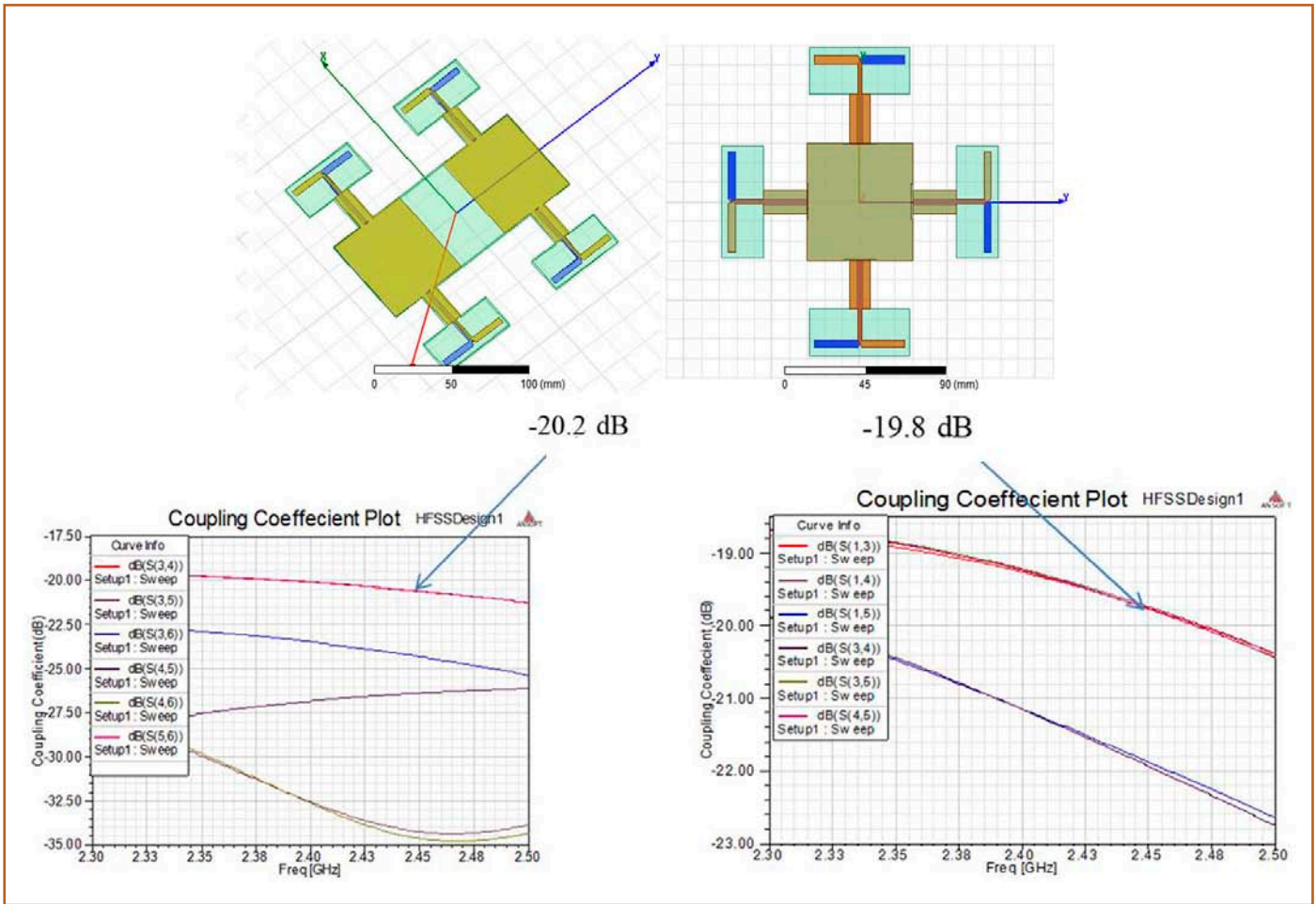Simulation results for parallel and plus are shown in Figure 5

Figure 5: PCB dipole based quad antenna (top) with coupling coefficient (bottom) for parallel & plus pattern respectively

(bottom) respectively. It can be observed that at 2.45 GHz, cross coupling is found to be higher in case of plus pattern quad antenna (-19.8 dB). Hence, parallel pattern quad antenna (cross-coupling -20.2 dB) has been chosen to be integrated with quad WCM. It is to be noted that, coupling effect is less in parallel antenna not only with respect to plus, but also with respect to directional patch based quad antenna. Figure 6 shows all fabricated antennas.

In this project, the design of different types of patch antennas such as rectangular patch, rectangular patch with DGS, meander with and without stub matching and PCB dipole antenna were demonstrated. Results are compared and PCB dipole is found to be the best suited candidate for designing quad antenna with bandwidth 300 MHz and gain 2.7 dB. Different spatial configurations of the suitable patch element have been explored and subsequently, cross coupling was minimized. It is also observed that the opposite patch elements are more coupled. Hence, PCB dipole based quad antenna with parallel pattern is more suitable for WCM application.

At present, the developed multi-channel sniffer is limited to capture data from 4-channels simultaneously. This design can be enhanced in future to capture data from all 2.4 GHz ISM channels.

Figure 6: Fabricated antennas

Young Researcher's Forum

Nano-spectroscopic and Nanoscopic Imaging of Single GaN Nanowire

Dr. Santanu Kumar Parida obtained his M. Sc degree in Physics with the specialisation in Solid State Physics from Utkal University, Bhubaneswar in the year 2014. He joined IGCAR as a research scholar in the year 2014 and carried out his research work in Surface and Nanoscience Division. He was awarded Ph. D. degree in Physical Sciences from Homi Bhabha National Institute in the year 2019. His doctoral research work is mainly focussed on the growth of III-V nitride nanostructures and study the localized optical electronic and electrical properties. His current research interest is to study the physical properties at nanoscale using scanning probe microscopic based techniques.

According to Abbe's criterion, the achievable spatial resolution in optical spectroscopy or microscopy is given as $\Delta x = 0.61\lambda/NA$, where λ is the wavelength of the probing laser and NA is the numerical aperture of the optical system. For the best practical conditions, the experimental value of Δx turns out to be about half of the wavelength. In the case of studies at the nanoscale, the optical spatial resolution limit prohibits a precise characterization of objects smaller than the diffraction limit. Therefore, the spectroscopic techniques provide ensemble-averaged information with lack in spatial resolution for nanoscale characterization. However, tip-enhanced Raman spectroscopy (TERS) is capable of performing such characterization as it couples the intrinsic spatial resolution of scanning probe microscopy (SPM) techniques with the chemical information collected from the vibrational spectroscopy. A metal-
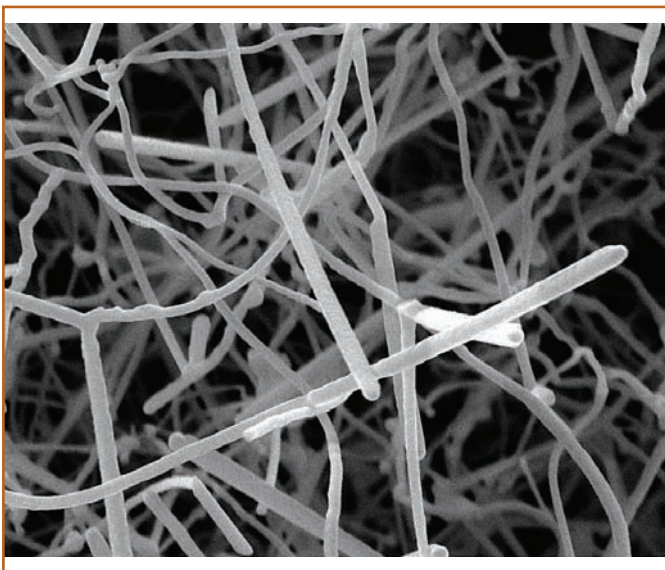
coated SPM tip or metal nanoparticle (NP) attached to the SPM tip allows nanoscale investigation of vibrational properties with the high spatial resolution because of enhanced and confined electromagnetic field at the tip apex or around the metal NP. Similarly, in the context of optical microscopy, light (visible to the mid-infrared regime of the electromagnetic spectra) covers the energies corresponding to the electronic transitions in atoms and molecular vibrations. Therefore, by using optical microscopes, one can get information related to the intrinsic properties of the materials. Nevertheless, the resolution attainable with an optical microscope is restricted by the diffraction limit of light. The diffraction limit can be overcome by using the plasmonic metal overlayered dielectric aperture of subwavelength size. Because of light confinement, the evanescent field is produced near the sub-wavelength aperture, and the availability of high spatial frequencies decreases exponentially with the distance from the aperture. Therefore, the object has to be kept in the near-field of the aperture and can be achieved by employing the SPM. In the near-field scanning optical microscopy (NSOM), the spatial resolution is dependent on the size of aperture rather than the wavelength of the illuminated light, and hence, the optical imaging of a sub-wavelength object can be easily achieved by raster scanning of the NSOM tip.

In the present report, we study the spectroscopic and optical imaging of single GaN nanowires (NWs) in the sub-diffraction limit. Raman spectroscopic imaging of single GaN NW (diameter ~200 nm) is demonstrated with the help of TERS. Similarly, the nanoscopic optical imaging of GaN NWs of ~10s of nm is also accomplished with the help of plasmonic (Au thin film) assisted NSOM technique in the sub-diffraction limit.

Experimental setup for the imaging

The GaN NWs were grown by catalyst assisted vapor-liquid-

Figure 1: FESEM micrograph of as-grown GaN nanowires with a large size distribution of diameter and length.

solid (VLS) process using atmospheric pressure chemical vapor deposition technique. For the spectroscopic study, the as-grown NWs were dispersed on single-crystal Al(100) substrate to get mono dispersed NWs. TERS measurements were carried out by scattering-type near-field spectroscopy using the scanning probe microscopy setup (Nanonics, MultiView 4000) coupled with the Raman spectrometer (inVia, Renishaw) in the backscattering configuration. A bent glass probe with Au particle (diameter <100 nm) attached to the tip was used as an aperture-less TERS tip for simultaneous AFM and spectroscopic imaging with the help of 514.5 nm laser excitation. The scattered light was collected using a 50X objective with an NA value of 0.42 and was dispersed through a grating of 1800 gr/mm to the charged coupled device detector. The simultaneous topographic and spectroscopic images of a single GaN NW were recorded by scanning the NW in the near-field. The spectral maps were created by integrating the intensity of the Raman modes collected at each point. The optical imaging at the nanoscale was carried out by aperture based NSOM in the reflection mode with 532 nm laser excitation. An Au/Cr metal overlayered aperture tip (~150 nm) was used for the near field scanning. The light from the laser source and aperture probe were coupled through an optical fiber. The scattered light from NWs was collected using far-field confocal microscope mounted with a 50X objective lens of the NA ~0.42. The collected light was directed towards the avalanche photodiode. The simultaneous topographic image was also acquired along with the NSOM maps.

Morphological studies

The typical FESEM micrograph of the as-grown GaN NWs [Figure 1] shows poly-dispersed NWs having diameter varying from ~ few 10s to 100s of nm, with a length of few microns. The as-grown NWs were dry-dispersed onto Al(100) substrate for the Raman measurements. The Raman spectra were collected for several single NWs. However, the NW with diameter ~200 nm could provide measurable Raman signal and was considered for further measurements.

TERS assisted nano-spectroscopic studies and imaging

The Raman spectra were collected for the selected single NW (diameter~200 nm as shown later from the AFM image) in the presence (with) and absence (without) of the TERS tip. In the Raman spectra [Figure 2], the prominent peaks ~568 and 560 cm^{-1} correspond to E_2(high) and E_1(TO) phonon modes, respectively. In the presence of TERS tip, the overall strength of the Raman spectra is increased, which is attributed to the enhancement of Raman scattering efficiency with the enhanced localized electric field in the near-field region of the TERS tip. The enhancement in the Raman signal for the E_1(TO) mode appears to be higher as compared to E_2(high) mode [Figure 2]. To investigate it further, the Raman spectra collected in the presence and absence of TERS tip at a single scan area on the NW were deconvoluted [Figures 2b and 2c]. After the deconvolution of the Raman spectra, a broad peak ~540 cm^{-1} was observed in both the cases and is assigned to the A_1(TO) vibrational mode. Further, the intensity ratio of all the three modes of A_1(TO), E_1(TO) and E_2(high) were calculated with the presence and absence of the TERS tip and was found to be 1.43, 2.08 and 1.65, respectively.

The enhancement factor in TERS is given by the relation,

$$EF = \left(\frac{I_{NF}}{I_{FF}} - 1\right) \frac{V_{FF}}{V_{NF}}$$

where I_{NF} and I_{FF} are the Raman peak intensities recorded with the presence and absence of TERS tip in the near- and far-field respectively. V_{FF} is the interaction volume of the far-field laser probe, and V_{NF} is the effective interaction volume of near-field TERS probe. A cylindrical interaction volume was considered and is given as $V = \pi(d/2)^2 \times \delta$, where δ is the depth of penetration. The enhancement factor for E_1(TO), E_2(high), and A_1(TO) are found to be around 31, 20 and 13, respectively. A low E_F value in case of GaN can be understood from the partial ionic nature leading to an insignificant change in the polarizability of the compound. Nominally higher enhancement factor was found for E_1(TO), as compared to E_2(high) and A_1(TO) modes. In the case
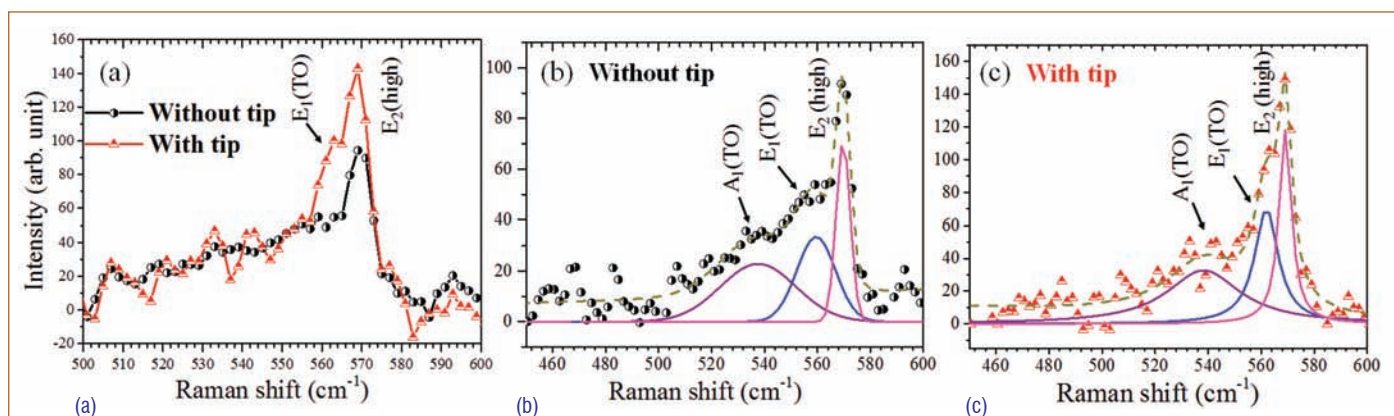

Figure 2: (a) Raman spectra of a single GaN nanowire with and without tip. Deconvoluted Raman spectra collected at a single scan area on the GaN nanowire (b) without and (c) with the assistance of TERS tip.

of wurtzite crystal, the direction of E_1 and E_2 mode vibrations are perpendicular to the *c*-axis of the crystal. However, A_1 vibrational mode is along the *c*-axis. It is well known that the field enhancement takes place for the electric field component parallel to the tip axis in case of the Si tip coated with Au or Ag. Therefore, there is a possibility of selective enhancement of the Raman modes whose vibration direction is parallel to the tip axis. However, in the present study, we have used a bent glass probe with a Au nano ball attached at the tip. Because of the symmetric nature of the Au nano ball, we do not observe any selective enhancement of the Raman modes. Therefore, we have observed a similar order of enhancement factor for all the Raman modes, even though their vibrational directions are different. However, the comparatively higher *EF* values observed in case of E_1(TO) as compared to that of E_2(high) can be attributed to the polar nature of the E_1(TO) mode.

In order to investigate further, the electric field distribution for the TERS set up is mapped by the FDTD method. The schematic of the simulated structures projected in *XZ* plane is shown in Figure 3(a). We consider the near-field spatial distribution of electric field intensity at the tip and NW interface and as shown for *XY* [Figure 3(b), *XZ* [Figure 3(c)] and *YZ* [Figure 3(d)] planes. From the intensity map, it is clear that the field strengths are of similar values

in all the planes. Therefore, TERS enhancement of all the modes is found to be of the same order.

The nano-spectroscopic imaging of single GaN NW was performed by scanning a single GaN NW placed under a fixed position of TERS tip in the vicinity of the incident laser beam. The spectroscopic map of a single NW was generated by considering the intensity of E_2(high) mode, which is dominant over others, along with the corresponding topographic information of the NW [Figure 4(a)].

The diameter of the NW was measured as 200 nm, as shown in the line profile of the height map of the AFM image [Figure 4(b)]. Since the NWs were grown via Au catalyst assisted VLS process, the AFM image [Figure 4(a)] of the NW contains the Au NP at the tip of the NW. Whereas, in the case of the TERS imaging [Figure 4(c)], the figure represents the intensity distribution of E_2(high) phonon mode of GaN NW. One can clearly see the direct correlation between the TERS and topographic images. However, the missing correlation between TERS and topographic image at the end of the NW is attributed to the absence of phonon mode for the Au NP [Figure 4(a)]. In the present configuration, the spatial resolution is restricted up to ~750 nm using 514.5 nm excitation and objective of ~0.42 NA. Moreover, the high fractional ionic
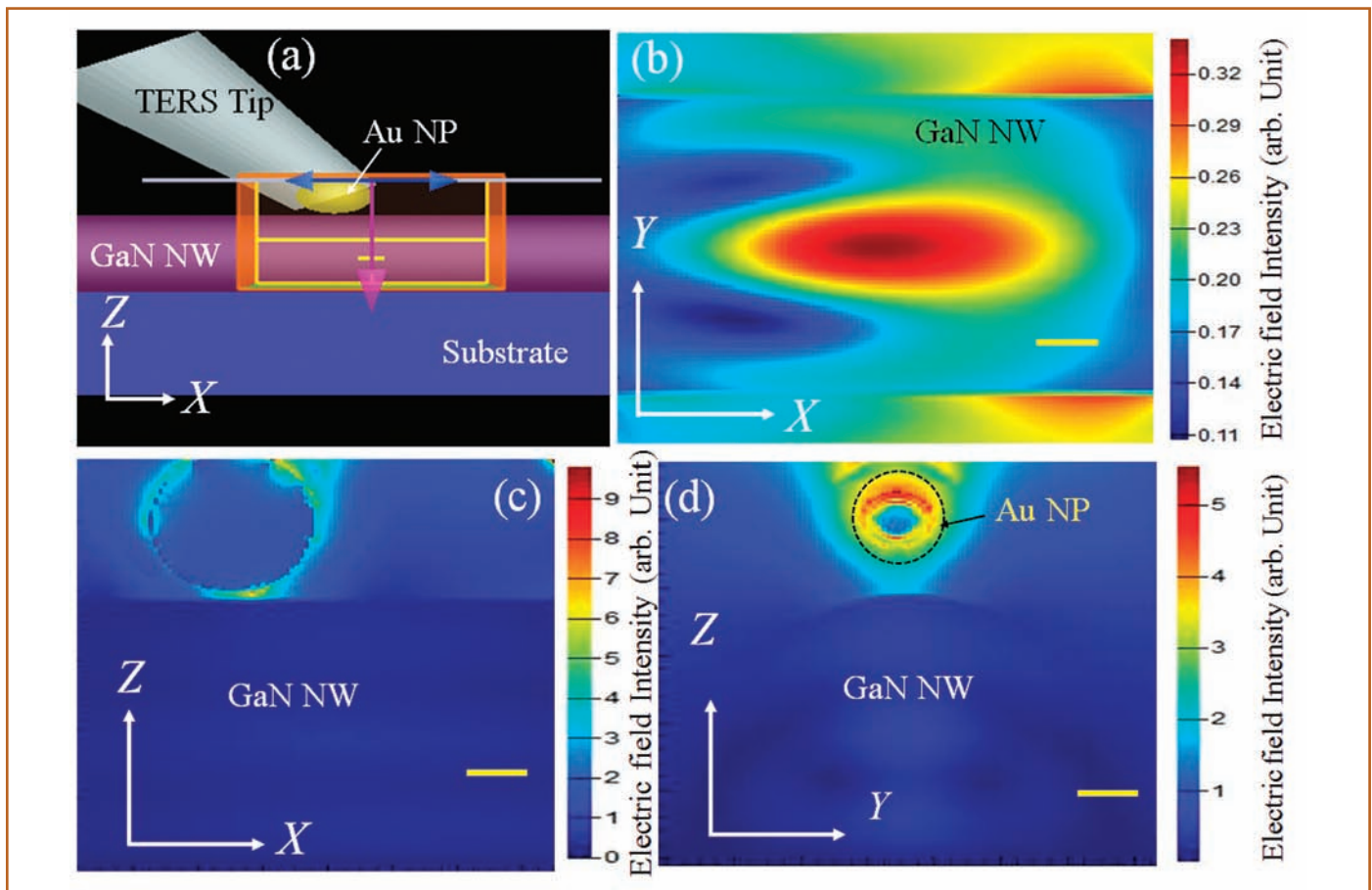

Figure 3: (a) The schematic view of the FDTD simulated structure along with *XZ* plane. The spatial distribution of the electric field intensity in (b) *XY* (c) *XZ* and (d) *YZ* planes. Scale bars are 40 nm. The color bars indicate the relative strength of the electric field intensity.
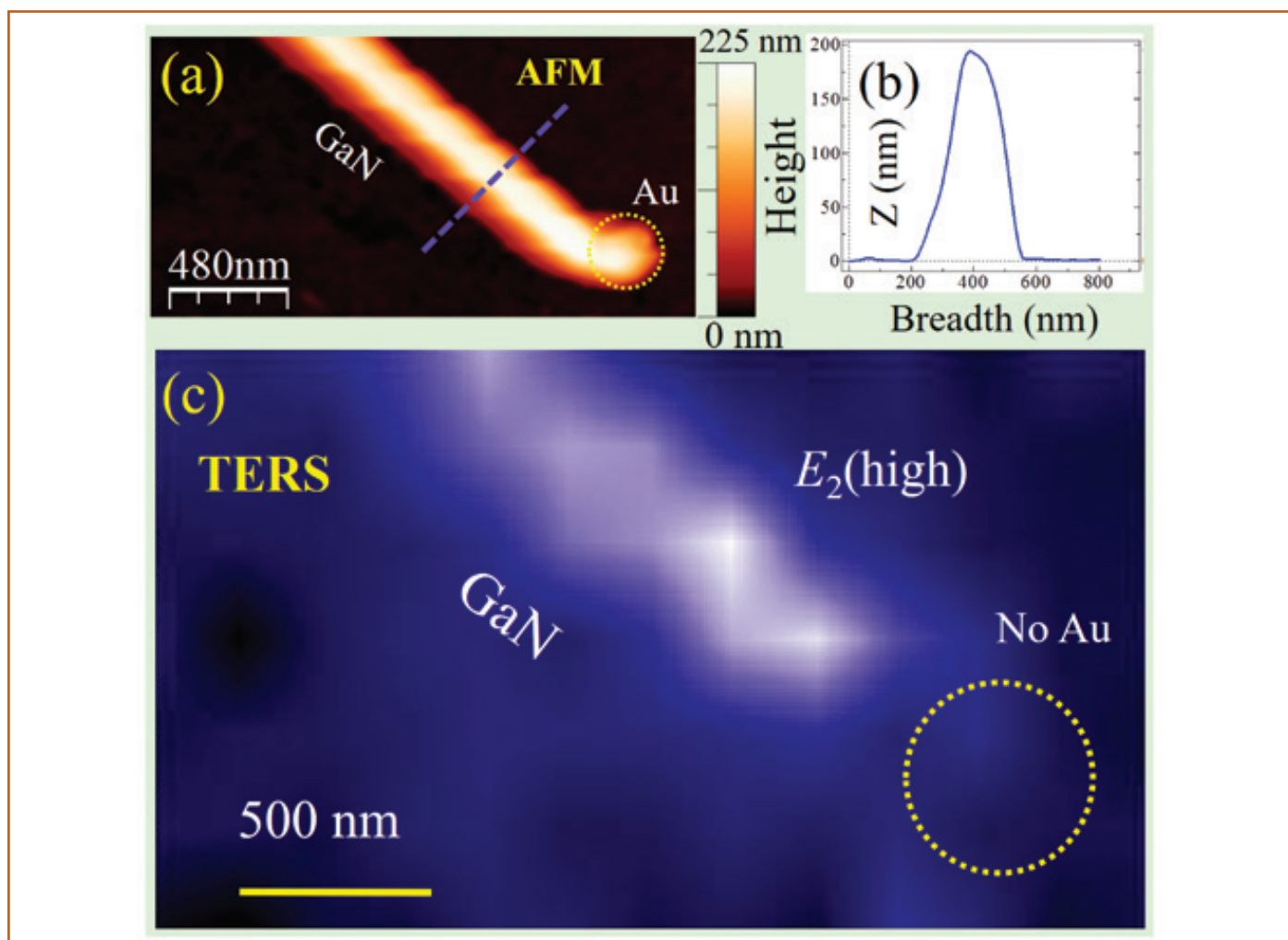
Figure 4: (a) AFM image of a single GaN NW with the corresponding (b) line profile showing the height of the NW as ~200 nm (c) The corresponding TERS image of the single NW mapped with the intensity distribution of the E_2 (high) mode.

character (FIC) and low scattering efficiency of III-nitride materials make it more challenging to image the single nanostructure using TERS. Generally, the signal to noise ratio in a single spectra can be improved by large exposure and acquisition times of incident and scattered radiation, respectively. However, spectral resolution can not be achieved in this process. This procedure is only helpful in studying the single nanostructure by collecting point-spectra along with the structure in the sub-diffraction limit. However, for spectroscopic imaging by TERS with the sub-diffraction resolution, it requires larger mapping time, which is one of the main constraints for using TERS as a regular characterization tool for single nanostructure imaging. During such large mapping times, the sample instability, drift and defocus in the incident laser beam position on TERS tip make it difficult to image the nanostructure with sufficient signal to noise ratio and appreciable contrast generation in the mapping. By minimizing the losses in scattered radiation and by collecting it more efficiently, it is possible to acquire better signal to noise ratio in the mapping, and hence faster imaging. To achieve

this condition, we have tested several metal substrates such as Au (150 nm Au film on high quality fused silica cover glass), Cu (100), Al(100)) and selected the Al substrate for TERS mapping of single GaN NW. However, with the help of TERS and choosing proper substrate (Al), we could study the spectroscopic property of a single GaN NW with a diameter ~200 nm far below the diffraction limit.

NSOM assisted nanoscopic imaging

Along with spectroscopic imaging, the optical micrograph also describes the intrinsic material property. However, the spatial resolution of the optical imaging is also restricted by the diffraction limit of a confocal microscope. In the present study, we intend to explore the nanoscopic imaging of GaN NW in the sub-diffraction limit. The nanoscopic near-field optical imaging of GaN NWs is carried out along with simultaneous AFM imaging. In the present study, "near-field excitation and far-field collection" configuration was employed for acquiring the NSOM signal. The sample was
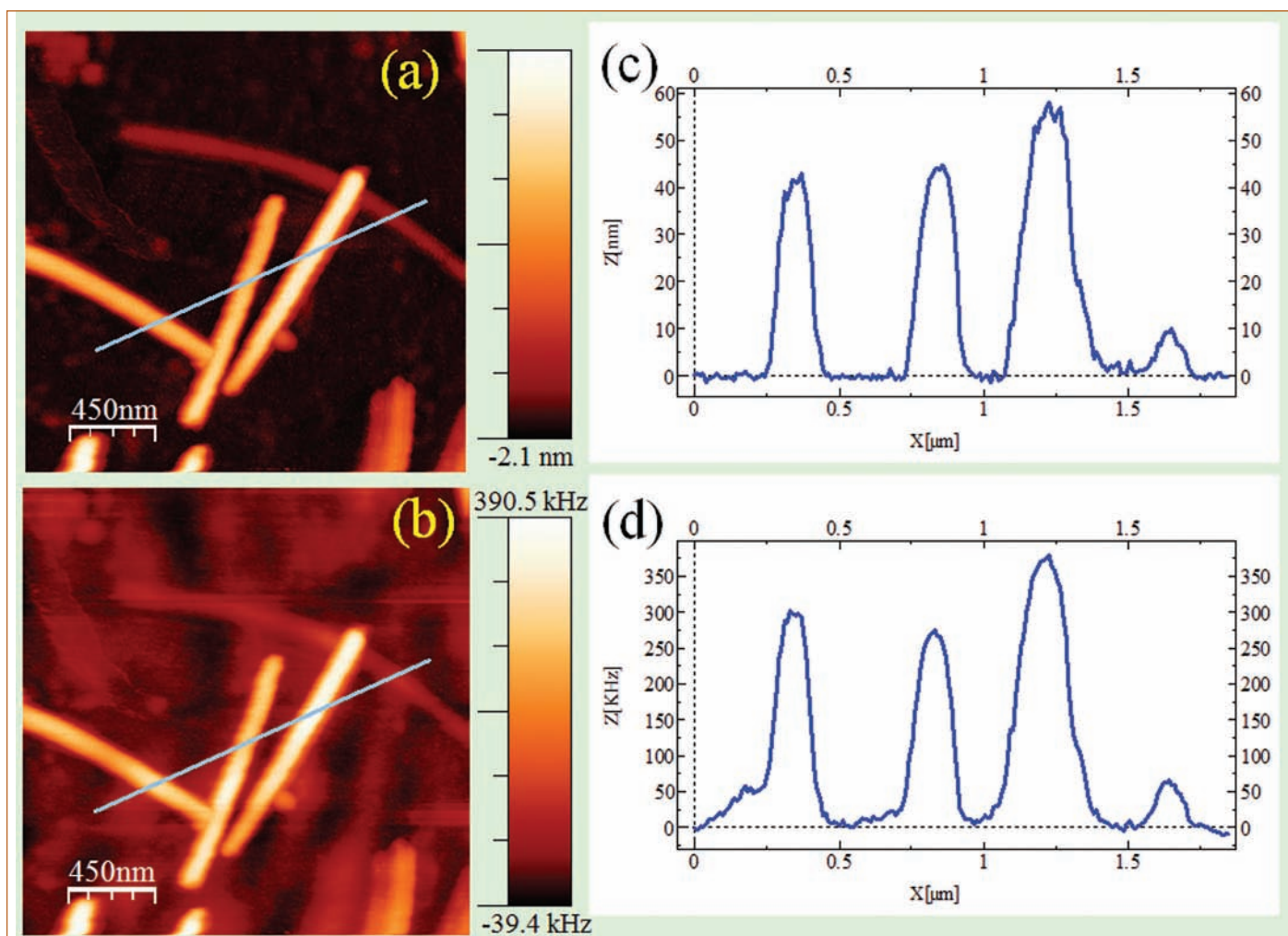
Figure 5: (a) Topographic and (b) NSOM image of GaN NW with diameter in the range of ~10-60 nm. The corresponding line profile of (c) topographic and (d) NSOM image in order to show the exact diameter.

kept in the near-field of the aperture probe, and the Rayleigh scattered photons were measured at the far-field with the help of a photo detector. NSOM image collected in this configuration is the spatial distribution of the Rayleigh scattering intensity. The AFM image with the corresponding NSOM image is depicted in Figure 5. The topographic AFM image shows NWs of smooth and cylindrical shape, with the diameter varying between 10 - 60 nm [Figure 5(a)]. As one can see, there is one to one correspondence between the AFM and NSOM image [Figure 5(b)]. All the NWs are resolved by both AFM and NSOM imaging with an aperture probe of ~150 nm. The NWs imaged in the present study are far below the diffraction limit for the excitation wavelength of 532 nm. Here, we intend to mention that even the smallest GaN NW (~10 nm) is also well resolved in the optical image. Several measurements were carried for the NWs of different diameter. In order to achieve such highly resolved optical images [Figure 5], one needs to shorten the wavelength of probing light down to the sub-diffraction regime. The shortening of wavelength can be achieved by using metal-coated NSOM probe, which produce an evanescent wave of momentum higher than that of the original excitation wavelength. The evanescent waves originating from the NSOM probe aperture possess a group of wave vectors higher than the original excitation laser with different velocities (v), which is slower than the excitation wave velocity. Moreover, it preserves the frequency of the excitation wave. Hence, one can achieve super-resolution as well as spectroscopic information such as luminescence from the nanostructure below the sub-diffraction limit.

In summary, with the help of tip-enhanced Raman spectroscopy and nanoscopic near-field scanning optical microscopy (NSOM), we could study the properties of GaN NWs far below the diffraction limit. Nano-spectroscopic image of a single GaN NW with diameter ~200 nm is recorded using TERS measurements and by careful selection of the TERS substrate. The variation in the enhancement factors for different Raman modes is attributed to the direction of corresponding atomic vibrations and their alignment with respect to the enhanced electric field in the presence of TERS tip. In a nanoscopic measurement, GaN NWs of diameter ~ few 10s of nm were imaged with excellent optical contrast, as a significant achievement using NSOM measurements.

Conference and Meeting Highlights

ISNT Level II Certification Programme in Visual Testing
January 06-10, 2020

Participants of the ISNT Level II Certification Programme in Visual Testing

Indira Gandhi Centre for Atomic Research in collaboration with Indian Society for Non-destructive Testing (ISNT), Kalpakkam Chapter, conducted ISNT Level II Certification Programme in Visual Testing in accordance with IS 13805 requirements during January 06-10, 2020 at Quality Assurance Division (QAD) of Safety, Quality & Resource Management Group (SQ&RMG) IGCAR. Totally 26 participants from various organizations such as NPCIL-QA Directorate, QUEST Inspection Services, NAPS, BARCF and different groups of IGCAR had attended the Programme.

Shri S. Athmalingam, Associate Director, HSEG & Head, QAD, inaugurated the course on January 06, 2020. Seasoned visual testing experts Prof. O. Prabhakar, IIT Madras, Shri Mani Mohan, Former Head-NDT Labs, BHEL, Shri R. Subbaratinam, Ex IGCAR and officials from QAD delivered lectures on various topics related to Visual Testing. Practical Session was conducted by the experts from QAD, IGCAR. As part of the certification programme, both theory & practical examinations were conducted on January 10, 2020 and Dr. B. Venkatraman, Director, SQ&RMG, appointed by NCB, ISNT HQ, officiated as the external examiner.

Reported by

Shri S. Athmalingam, Associate Director, HSEG & Head, QAD

Conference and Meeting Highlights

All India Hindi Scientific Seminar (AIHSS-2020)
January 09-10, 2020

Inauguration of All India Hindi Scientific Seminar (AIHSS-2020) (L to R): Shri J. Srinivas, Dr. Awadesh Mani, Dr. Arun Kumar Bhaduri, Distinguished Scientist & Director, IGCAR & GSO, Shri Neeraj Sinha, Advisor (S&T), Niti Aayog, Dr. Kallol Roy, CMD, BHAVINI, Dr. B. K. Nashine and Shri O. T. G. Nair, Director (P&A)

The Official Language Implementation Committee (OLIC) of Indira Gandhi Centre for Atomic Research (IGCAR) and General Services Organization (GSO), Kalpakkam in collaboration with NITI Aayog, New Delhi and BRNS, Mumbai jointly organized a two day All India Hindi Scientific Seminar (AIHSS-2020) titled "Oorja Ke Kshetra Me Bharatiya Vigyan Evam Takniki Pragati" (Indian Scientific and Technological Progress in the field of Energy), during January 9-10, 2020. The Seminar was organized as part of promoting official language Hindi in Scientific and Technical writing. The event was inaugurated by Shri Neeraj Sinha, Advisor (S&T), NITI Aayog, New Delhi in the august presence of Dr. Arun Kumar Bhaduri, Distinguished Scientist & Director, IGCAR & GSO and Dr. Kallol Roy, CMD, BHAVINI. Besides the dignitaries, senior members of the OLIC, Shri O. T. G. Nair, Director (P&A), Dr. B. K. Nashine, Dr. Awadhesh Mani from IGCAR, were also present.

The Seminar comprised of five oral sessions and a poster session. Highlights of various scientific works performed in the areas pertaining to conventional & non-conventional sources of energy and associated technological advancements were discussed in the seminar. Around 150 delegates from BARC, HWB (Mumbai), NPCIL, NTPC (New Delhi), RMP & AMD (Bengaluru), NFC & ECIL (Hyderbad), RRCAT (Indore), NISER & IOP (Bhubneswar), VNIT (Nagpur), CBRI (Roorkee), VECC (Kolkota), besides BHAVINI, MAPS, BARCF, IGCAR & GSO from Kalpakkam, participated in the seminar. In addition to 12 invited lectures by eminent scientists and experts, nearly 50 papers were presented in poster and oral sessions. The cultural team of BARC, Mumbai presented two scientific skits depicting the importance of peaceful uses of atomic energy, in the evening of 09.01.2020. Best paper and poster presentations were awarded cash incentives. While the inaugural and main technical sessions were held in the Sarabhai Auditorium in IGCAR, the final and valedictory sessions were conducted at GSO, Kalpakkam.

Reported by

Shri O.T.G. Nair, Director (P&A)

Conference and Meeting Highlights

Workshop on "Planning, Preparedness and Response to Radiation Emergencies for Medical and Security Officers"
February 17-20, 2020

Participants of the workshop on "Planning, preparedness and response to radiation emergencies for medical and security officers"

A workshop on "Planning, preparedness and response to radiation emergencies for medical and security officers" was organized for the first time, at Health, Safety and Environment Group, SQRMG, IGCAR during February 17-20, 2020. The Workshop was inaugurated by Capt. Loganathan, Indian Navy, Kalpakkam. A total of 44 Officers including medical officers from southern naval units, DAE hospital, Kalpakkam and security officers from army and CISF at Kalpakkam participated in the four day workshop. Lectures on topics like planning, preparedness for effective response Role of Crisis Management Group, DAE and Role of Emergency Response Centre during nuclear and radiological emergencies, decontamination procedures, Medical management of radiation injuries etc., were delivered by faculty members from IGCAR, BARC and DAE Hospital. Technical visits were arranged for the participants to various radioactive facilities at Kalpakkam.

Major General PK Hasija, MG, MED, Dakshin Bharat Area, Chennai, was the chief guest in the valedictory function and participation certificates were distributed by him. In the valedictory address, he stressed upon the need for sharing the medical management experience to deal with nuclear and radiation emergencies. Dr. Prodip Bhattacharjee, MS, DAE Hospital, Kalpakkam participated as the guest of honour in the function.

Reported by
Dr. M. T. Jose, Head, HISD, SQRMG

Conference and Meeting Highlights

One Day Workshop on RFID Technology for Libraries
February 19, 2020

Dr. B. Venkatraman, Distinguished Scientist and Director, SQ&RMG & ESG addressing the gathering during the inaugural session

A one day Workshop on Radio Frequency Identification Technology (RFID) for Libraries was organized by IGCAR in association with Madras Library Association -Kalpakkam Chapter (MALA-KC) on 19-02-2020 at Sarabhai Auditorium, IGCAR, Kalpakkam. The objective of the workshop was to familiarize RFID technology and gadgets to Public Librarians in the neighbouring districts of Kalpakkam. Around 60 delegates including Librarians from academic and public domain, information technology professionals and Research Scholars attended the Workshop.

The Workshop was inaugurated by Dr. B. Venkatraman, Distinguished Scientist and Director, SQ&RMG & ESG, Smt. S. Prabavathi, Treasurer, MALA-KC welcomed the gathering. Dr. T. S. Lakshmi Narasimhan, Associate Director, Resource Management Group/SQRMG delivered the special address. Smt. S. Rajeswari, Head, Scientific Information Resources Division (SIRD) and President MALA-KC delivered the key note address on "Role of libraries in promoting digital services". Dr. B. Venkatraman, Director SQRMG and ESG released the new SIRD intranet portal (http://vaigai) and delivered the presidential address emphasizing the need for integrating digital technology in every aspect of library services. Shri E. Soundararajan, Secretary, MALA-KC, proposed the formal vote of thanks.

The Workshop included lectures by colleagues from SIRD in the field of RFID technology, KOHA based Library Management System and SIRD Digital Library Services. A separate hands-on session on RFID technology was also arranged. This workshop facilitated good interaction amongst the Librarians, students and professionals in the area of RFID technology and Integrated Library Management System.

Participants of the workshop

Reported by
Smt. S. Rajeswari, Head, SIRD

Conference and Meeting Highlights

4th Discussion Meeting with Collaborative Institutes/Labs on Indian AUSC Projects, Kalpakkam
March 02-03, 2020

The meeting was chaired by Shri S. C. Chetal, Ex-Director, IGCAR and AUSC Mission Director accompanied by Dr. Arun Kumar Bhaduri, Distinguished Scientist & Director, IGCAR and Dr. Shaju K. Albert, Director, MMG and MSG, IGCAR

IGCAR has been a consortium partner in the multi-agency R&D project "Development of Advanced Ultra-Super Critical (AUSC) technology for thermal power plants on a Mission Mode" approved by the Cabinet Committee on Economic Affairs (CCEA). The other two partners in the consortium are BHEL and NTPC. The multi-agency R&D mission project is being executed by the AUSC Mission Directorate under the Department of Heavy Industries (DHI), Government of India. In this project, there has been high emphasis on the use of indigenously developed materials and technologies for the Indian AUSC Power Plant.

Roles assigned to IGCAR in the Indian AUSC Consortium are advanced design analysis, materials development, manufacturing technology, testing and evaluation. Generation of material property data is an important part of the R&D phase of the AUSC project, and thus specific projects of relevance to the AUSC Mission have been identified by IGCAR and awarded collaborative projects under the national AUSC Mission to various Academic Institutes/National Labs for the evaluation of important material properties. The collaborative projects would also establish a National network of high temperature material testing infrastructure for carrying out future material testing and evaluation works related to the AUSC technology and other high temperature applications.

The collaborative projects are being reviewed every six months through presentations by the respective project investigators. The latest project review meeting, which is fourth in the series, was held during March 2-3, 2020 at IGCAR. About 35 faculties/ scientists from various Academic Institutes (IIT Bombay, IIT Kharagpur, IIT Bhubaneswar, IIT Roorkee, IISc Bangalore, VNIT Nagpur, NIT Warangal, Jadavpur University Kolkata and CSIR-NML Jamshedpur) had presented the status of projects. About 35 scientific officers from IGCAR and 2 officers from BHEL Corporate R&D, Hyderabad had also participated in the review meeting. The Two-day review meeting was chaired by Shri S. C. Chetal, Ex-Director IGCAR and AUSC Mission Director accompanied by Dr. Arun Kumar Bhaduri, Distinguished Scientist & Director, IGCAR and Dr. Shaju K. Albert, Director, MMG and MSG, IGCAR.

Reported by

Dr. Shaju K. Albert, Director MMG & MSG

Swachhta Pakhwada - 2020
February 16-28, 2020

Visit by the members of Swachhta Cell

News and Events

Certificate of appreciation was awarded by Shri M. S. Premnath, Superintending Engineer (Retired), Chennai Corporation for the best three clean locations during the closing ceremony of Swachhta Pakhwada.

Shri M. S. Premnath, Superintending Engineer(Retd.), Chennai Corporation & Shri S. N. Nandhagopal, Consultant & Expert (Pyrolysis of Plastic e-Waste Management) during the closing ceremony

Indira Gandhi Centre for Atomic Research observed "Swachhta Pakhwada" during February 16-28, 2020. During this period E-waste management and cleaning of surroundings within the plant site and cleaning of office premises were carried out.   In order to provide a boost to the swachhta activities, members of IGCAR Swachhta Cell visited various Divisions/Groups and selected three best kept locations in the Centre. Certificate of appreciation was awarded for the best three clean locations during the closing ceremony of Swachhta Pakhwada. Guest lectures by Shri M. S. Premnath, Superintending Engineer (Retired), Chennai Corporation on "Wealth from Garbage" and Shri S. N Nandhagopal, Consultant and Expert Pyrolysis on "Plastic E-Waste Management" were organized on the closing day. Essay, slogan and poster competitions on the topic "Cleanliness towards Nation's Development" were conducted and prizes were distributed to the winners during the closing ceremony.

Reported by

Shri O.T.G. Nair, Director (P&A)

Orientation Program for Engineers and Supervisors involved in Construction
February 21, 2020

A one day Orientation Program was organized on February 21, 2020 at Fast Reactor Fuel Cycle Facility (FRFCF) for engineers, supervisors, technicians, draftsmen and skilled assistants engaged in construction site works in various disciplines viz. Civil, Mechanical, Electrical, Instrumentation and Safety. Dr. B. P. C. Rao, Project Director, FRFCF inaugurated the event and explained the significance of this multi-unit mega project in realizing the goals of the department. He also highlighted the importance of integrity, quality and safety aspects in the work carried out.

HBNI-IGCAR Corner

Ph.D Thesis Defense

Name	Title	Date	Discipline
Shri Amit Kumar Mishra	Studies on Nano-Inclusion Assisted Enhancement in Thermal Conductivity and Photo-Thermal Conversion of Organic Phase Change Materials	20.01.2020	Chemical Sciences
Ms. K. S. Sree Ranjini	Design, Development and Optimization of High Temperature Motors for In-Service Inspection Devices	03.02.2020	Engineering Sciences
Shri G. Padmanabhan	Studies on Deep Excavation Behaviour in Engineered Backfilling Adjacent to Nuclear Safety Related Structures.	06.03.2020	Engineering Sciences
Ms. Raktima Basu	Mechanism of Phase Transition in Vanadium Oxides and its Applications	14.01.2020	Physical Sciences
Ms. A. N. Arpita Aparajita	Synthesis and Studies of Transition Metal Borides and Carbides under High Pressure	20.01.2020	Physical Sciences
Ms. Madhusmita Panda	Synthesis and Characterization of Diamond Like Carbon (DLC) Based Nano-composite Thin Films Grown by PLD	04.02.2020	Physical Sciences
Ms. Sithara Vinod	Studies on the Effect of Magnetic Field Induced Aggregation on Physical Properties of Ferrofluids	21.02.2020	Physical Sciences

Awards and Honours

Dr. Hara Prasanna Tripathy, PMD, MCG / MMG , was awarded the Young Scientist award for the year 2019 by Indian Thermal analysis Society (ITAS).

Dr. Raj Narayan Hajra, PMD, MCG / MMG was awarded the ITAS-SETARAM Calorimetry award for the year 2019 by Indian Thermal analysis Society (ITAS).

Dr. Chanchal Ghosh, PMD, MCG/MMG was awarded 'EMSI-Excellence in Microscopy' by Electron Microscopy Society of India.

Best Paper/Poster Awards

International Conference on Nano Science and Technology (ICONSAT 2020) , March 5 -7, 2020, Biswa Bangla Convention Centre, New Town, Kolkata.
Effect of Magnetic Field Ramp Rate on Microstructure Formation in Magnetic Nanoemulsion
Dillip Kumar Mohapatra and John Philip
Best Poster Award

National Symposium on Recent Advances in Chemistry, (NSRAC 2020) February 18-19 2020, Pondicherry University
Synthesis of Water Based Fe_3O_4 Nanoparticles by Oxidation - Precipitation and its Application in Removal of Methylene Blue Dye
C Anushree and John Philip
Best Paper Award

Biodiversity Basket - Avian Fauna

Brown Shrike

Brown Shrike is a predatory bird with a strong stout bill, hooked at the tip. It has strong legs and feet, a large head and a long tail with graduated tip. It has rufous-brown crown, nape and tail whereas its lower forehead is creamy white. The bird has distinctive black bandit mask through eye to rear ear-coverts. Conservation status is 'Least Concern' but population is declining.